

# Charge Carrier Transport in Bulk Heterojunction Solar Cells

## Bachelor Thesis

to obtain the academic degree

Bachelor of Science (BSc.)

in the Bachelor program

Technical Chemistry

**Author:**

Nikolas Heitzmann

**Prepared at the:**

Institute of Physical Chemistry - Linz Institute for Organic Solar Cells (LIOS)

**Thesis supervisor:**

o.Univ. Prof. Mag. Dr. DDr. H.c. Niyazi Serdar Sariciftci

**Guidance:**

Assoc. Prof. DI Dr. Markus Clark Scharber

Linz, 30<sup>th</sup> May, 2017

## **Statement of Authorship**

I hereby declare this bachelor thesis was entirely written by me and without foreign help. No other person's work has been used without due acknowledgement in this thesis. All used references are cited in the bibliography in all conscience.

Linz, 30<sup>th</sup> May, 2017

---

Nikolas Heitzmann

## **Kurzfassung**

Das Ziel dieser Arbeit ist die Herstellung von funktionsfähigen Solarzellen von P3HT Poly(3-hexylthiophen-2,5-diyl) und P3HT/PCBM (Phenyl-C61-butyric acid methyl ester), die auf ihren Wirkungsgrad als auch auf die Beweglichkeit der Ladungsträger mittels Photo-CELIV, bei verschiedenen Temperaturen, untersucht werden. Es werden drei Solarzellen mit einem unterschiedlichen Anteil an PCBM hergestellt, um die Auswirkungen des Akzeptors auf den Ladungstransport zu studieren. Zusätzlich wird die Diffusionsspannung der Zellen mittels Impedanzspektroskopie bestimmt.

## **Abstract**

This work aims to process simple solar devices from P3HT (Poly(3-hexylthiophen-2,5-diyl)) and P3HT/PCBM (Phenyl-C61-butyric acid methyl ester), which are further characterized in terms of efficiency and the mobility of the charge carriers with the photo-CELIV technique under different temperatures. Three devices with a different content of PCBM are measured to investigate the contribution of the PCBM to the charge carrier transport. In addition, the built-in voltage of these devices is determined by impedance spectroscopy.

## Table of Content

1. Introduction.....	5
2. Theoretical background.....	6
2.1 Bulk heterojunction solar cells .....	6
2.2 Photo-CELIV .....	8
2.3 Impedance spectroscopy .....	10
2.3.1 Schottky contact .....	11
2.4 Poole-Frenkel field dependence .....	12
3. Experimental Section .....	14
3.1 Production procedure.....	14
3.2 Equipment.....	16
3.2.1 Cryostat .....	16
3.2.2 Installation of the solar cell .....	16
3.2.3 Apparatus for Photo-CELIV measurements .....	18
4. Measurements and results .....	20
4.1 Pure P3HT-film .....	20
4.1.1 JV characteristics of a pure P3HT film.....	20
4.1.2 Mobility in P3HT films.....	21
4.1.3 Charge carrier concentration in P3HT films .....	25
4.2 P3HT/PCBM (0.95:0.05) Bulk Heterojunction Solar Cell.....	27
4.2.1 JV characteristics .....	27
4.2.2 Mobility.....	28
4.2.3 Charge carrier concentration .....	31
4.3 P3HT/PCBM (1:1) Bulk Heterojunction Solar Cell.....	33
4.3.1 JV characteristics .....	33
4.3.2 Mobility.....	34
4.4.3 Charge carrier concentration .....	37
4.4 Impedance spectroscopy: Mott-Schottky plot .....	39
4.5 Poole-Frenkle field dependence of all devices .....	40
5. Conclusion .....	41
6. Bibliography .....	43
7. Acknowledgements.....	44

## **1. Introduction**

The world's energy consumption is increasing with every year, which leads to a higher demand for sustainable technologies to produce and store energy. Besides various green energy sources like energy from wind and water, it is believed that solar technology will fulfil the energy demands in the future.

Today, a broad market for commercially available photovoltaics has already been established. However, commercial photovoltaics are often produced with polycrystalline silicon, which makes them bulky and heavy. Another concept for solar energy is represented by the organic photovoltaics (OPV). Instead of polycrystalline silicon, organic semiconducting materials are utilized. The major advantage of this technology is that the required materials can be produced fairly cheap and the material amounts that are used for production are rather small. Organic photovoltaics are produced via solution processing, which enables them to be printed [1] as thin films onto plastic substrates. This enables them to be manufactured on a large scale while maintaining low costs. The simplified production procedure, flexibility and good absorption of light, enables various applications for OPV in our day-to-day life. Advances in solar photovoltaics are needed to increase the performance of organic solar cells and make solar harvesting more available at a lower cost. [2]

## **2. Theoretical background**

### **2.1 Bulk heterojunction solar cells**

The first concepts of organic solar cells reach back to the late 1950s. A breakthrough of this technology was achieved in 1986 when Tang combined donor and acceptor materials. This concept of heterojunction has been used and was further improved until today. [3]

Organic semiconductor materials are used in organic solar cells because of their various advantages and their high potential. Carbon-based materials, such as semiconducting polymers, can be easily processed since they do not require a complicated synthesis, which makes them cheap. In addition, those polymer molecules can be chemically tailored to increase the absorption or to alter the band gap. Since the absorption of semiconducting polymers in photovoltaic devices is high, the active layer of the device only needs to be a few hundred nanometers thick.

A key role of organic semiconductor materials lies within the simple fabrication of devices and the possible mass production of those. These materials can be dissolved in an organic solvent and blended with other materials to enable a wet processing of organic solar cells [1]. Combined with a roll-to-roll fabrication very thin devices can be produced on various types of substrates like glass or thin plastic foil with an overall low material consumption. The printing of organic solar cells on thin and flexible substrates leads to a new branch of technological applications, such as smart-applications on cars or implementations in garments.

The active layer of a bulk heterojunction solar cells is made of donor and acceptor molecules. The donor usually consists of conjugated polymers, whereas the acceptor frequently consists of fullerene derivatives. The combination of the donor and acceptor molecule enables a good charge transfer and has increased optical properties.

When a photon with an equal or higher energy than the band gap of the donor is absorbed, then a transmission of an electron from the highest occupied molecular orbital (HOMO) to the lowest occupied molecular orbital (LUMO) level takes places. The excitation of an electron leaves an electron hole in the HOMO. This electron-hole pair is called an exciton. Electrical current is obtained by separating this exciton and extracting the free charges by transporting them to the cathode and anode. However, an exciton can only diffuse 10 nm [4] in its lifetime. If the exciton does not reach the donor acceptor interface it will recombine, which leads to no power generation inside the solar cell. The donor material is used for efficient separation of

the exciton, since the coulomb binding in organic materials is very high because of the low dielectric permittivity ( $\epsilon = 3$ ). As displayed in figure 1, the excited electron in the LUMO-level of the donor is transferred to the lower lying LUMO-level of the acceptor, which leads to a weaker attraction of the exciton. After separation, the charges are transported to the electrodes. [5]

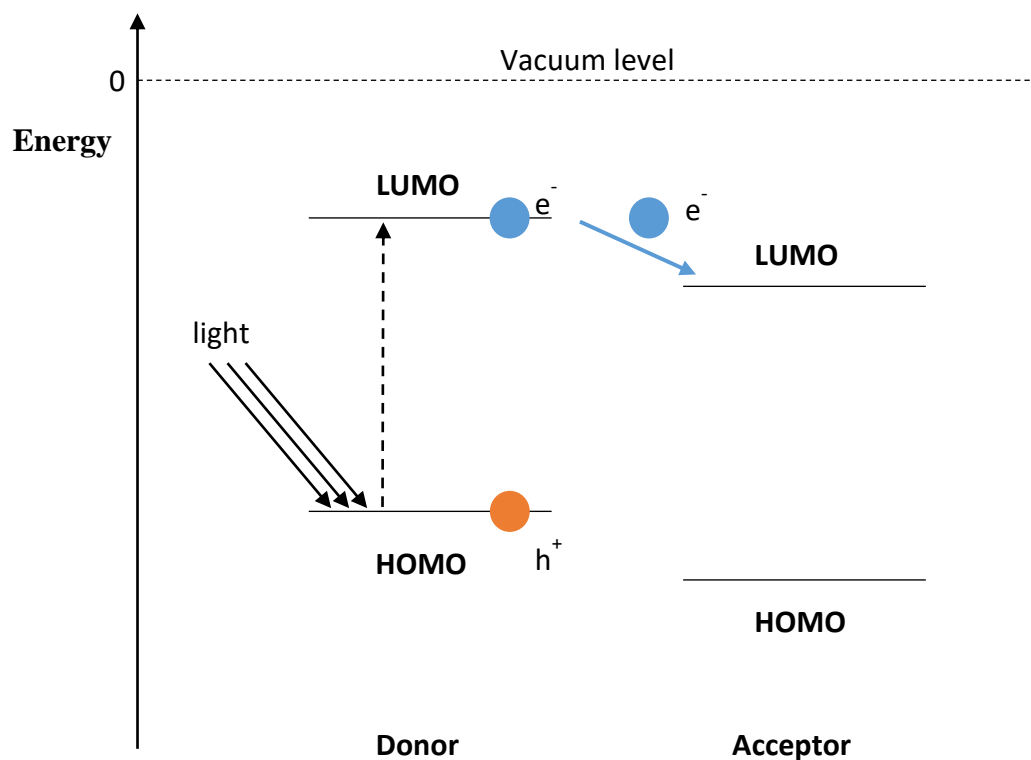


Figure 1: Working principle of a donor-acceptor interface in organic solar cells.

The improvement of the donor/acceptor interface is substantial, since the generated exciton can only be separated there before recombination. The bilayer arrangement has a donor/acceptor interface, where the excitons only have a limited interface for separation. Other excitons, which are generated outside the diffusion range of the interface, cannot be separated and will therefore recombine. By using a solution processing method of the active layer, where the donor and acceptor materials are highly mixed, the donor/acceptor interface is further increased. Both arrangements can be seen in figure 2. [5]

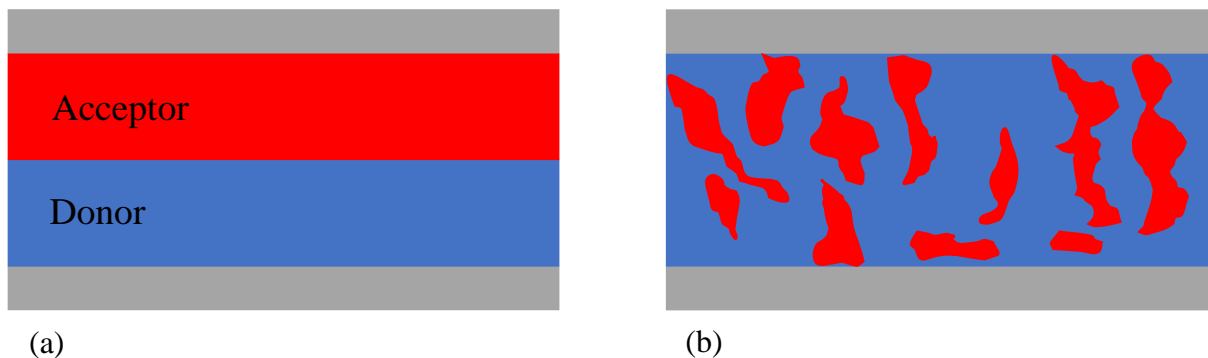


Figure 2: Theoretical schematic of a donor/acceptor interface of a bilayer arrangement between two electrodes (a) and an improved highly-intermixed donor/acceptor interface (b).

## 2.2 Photo-CELIV

The CELIV technique was introduced by Juška et al. [6] in 2000 and allows besides other techniques like TOF (time of flight) and impedance spectroscopy, the characterization of the charge transport in organic semiconductors. The photo-CELIV method utilizes a linear increasing voltage in reverse direction to extract photo generated carriers, while the mobility is obtained from the peak maximum of the corresponding photo-CELIV signal. The photogeneration of additional charge carriers in organic semiconductors is pursued since the number of carriers are in general low. An advantage of the photo-CELIV technique is that it probes transport in samples with optimized fabrication conditions for real working devices in terms of active layer thickness and architecture. [7]

The mobility ( $\mu$ ) represents the transport of charge carriers inside an organic semiconductor material. In figure 3 a graph for the linear increasing voltage and the corresponding photo-CELIV signal is displayed.  $Q_E$  is the amount of charge carriers, which are extracted when a linear increasing voltage is applied. The charge carrier concentration ( $N$ ) is obtained by dividing  $Q_E$  by the active layer thickness.

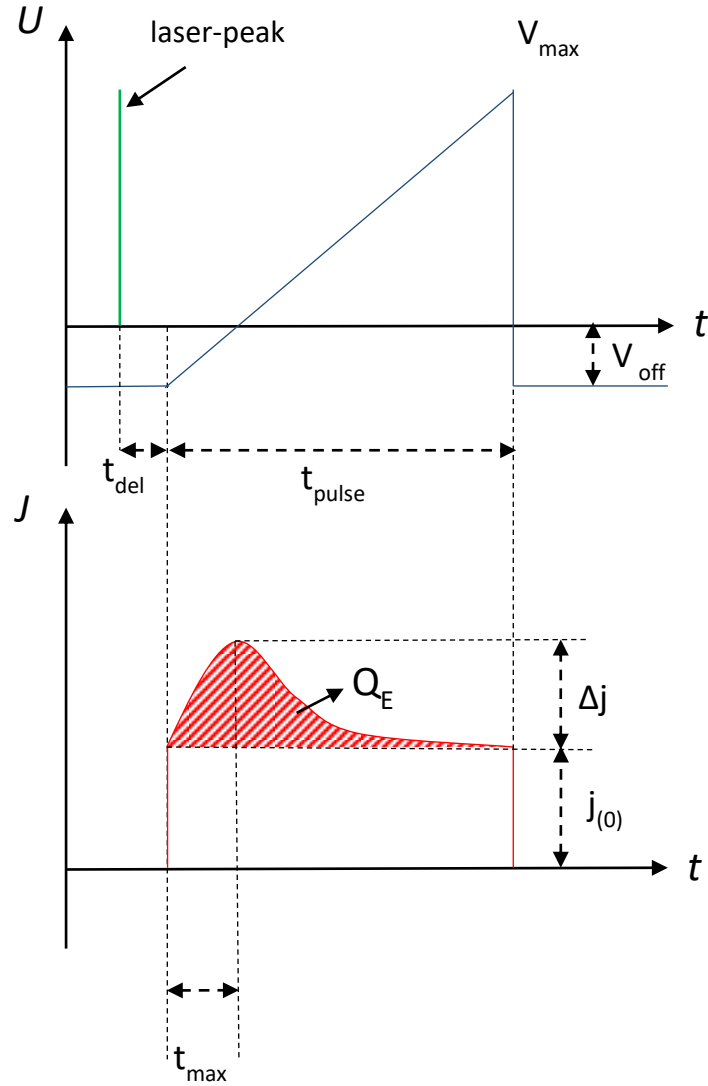


Figure 3: Depiction of the photo-Celiv technique. Top diagram shows the applied voltage ramp in reverse direction. Bottom diagram shows the corresponding photo-CELIV signal.

If no free charge carriers were extracted, then only a rectangular shape with the height  $j(0)$  would be observed. The red marked area  $Q_E$  represents the amount of charge carriers that are extracted through the applied electrical field by the linear increasing voltage in reverse direction. The height of  $Q_E$  is defined by the end of  $j(0)$  to the peak maximum and is called  $\Delta j$ . These values and other parameters like the delay between the laser-pulse and the extraction ( $t_{\text{del}}$ ), the voltage ramp duration ( $t_{\text{pulse}}$ ), the time between the extraction start and the peak maximum of  $Q_E$  ( $t_{\text{max}}$ ) and the offset voltage ( $V_{\text{off}}$ ) are important for the calculation of the mobility.

The following equation (1) [7] is used to calculate the mobility if  $\Delta j \approx j(0)$ .

$$\mu = \frac{2 d^2}{3 A t_{max}^2 \left[ 1 + 0.36 \frac{\Delta j}{j(0)} \right]} \quad (1)$$

In some cases the requirement of  $\Delta j \approx j(0)$  is not given. Therefore, another equation (2) [8] is utilized to calculate the mobility over a wide range of  $\Delta j/j(0)$  ratios.

$$\mu = \frac{d^2}{2 A t_{max}^2} \left[ \frac{1}{6.2 \left( 1 + 0.002 \frac{\Delta j}{j(0)} \right)} + \frac{1}{\left( 1 + 0.12 \frac{\Delta j}{j(0)} \right)} \right]^2 \quad (2)$$

In equation (2) the variable  $d$  stands for the thickness of the active layer and  $A$  is the slope of the linear increasing voltage ramp over time ( $V_{max} / t_{pulse}$ ).

### 2.3 Impedance spectroscopy

Impedance spectroscopy is a method, where resistance, capacitance and the inductance of an electronic device are characterized. This is achieved by applying a small AC voltage signal in addition to a DC bias, which gives an insight into frequency dependent relations inside the device. Besides the variation of the frequency, the applied DC bias voltage can also be modulated, which gives further information of the impedance at a specific bias voltage.

For measuring an organic solar cell an equivalent circuit has to be assumed to describe the complex processes inside the device. Usually the measured values are fitted with this theoretical equivalent circuit, which can consist of resistors and capacitors. In figure 4 a standard equivalent circuit, which is also used for the interpretation of the data in this thesis, is displayed. The circuit consists of a serial resistor  $R_S$  and a parallel resistor  $R_P$  and

capacitor  $C_P$ . The data is also interpreted in form of diagrams. A frequently used way to determine the built-in voltage of an organic solar cell is to create a Mott-Schottky plot. [9]

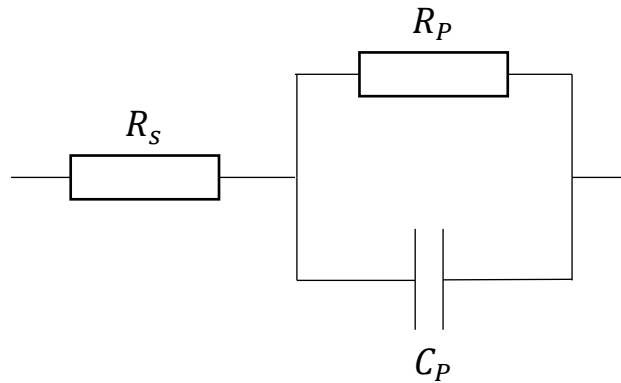


Figure 4: Equivalent circuit, which is used to interpret the impedance data.

### 2.3.1 Schottky contact

The interface between a metal and a doped semiconductor is referred to as a Schottky contact. The Schottky contact describes the depletion of charge carriers between the metal-semiconductor interface when a built-in potential is present.

In figure 5 the energy band diagram of a metal and a p-doped semiconductor is displayed. The Fermi level ( $E_{F,m}$  in figure 5 (a)) of the metal is higher compared to the Fermi level of the doped semiconductor ( $E_{F,sc}$ ), which lies between the valence band ( $E_V$ ) and the conduction band ( $E_C$ ). As a consequence, the work function of the metal  $\phi_m$  is smaller than the work function of the semiconductor  $\phi_{sc}$ , which is given by the difference between the Fermi level and the vacuum level. [9] [10]

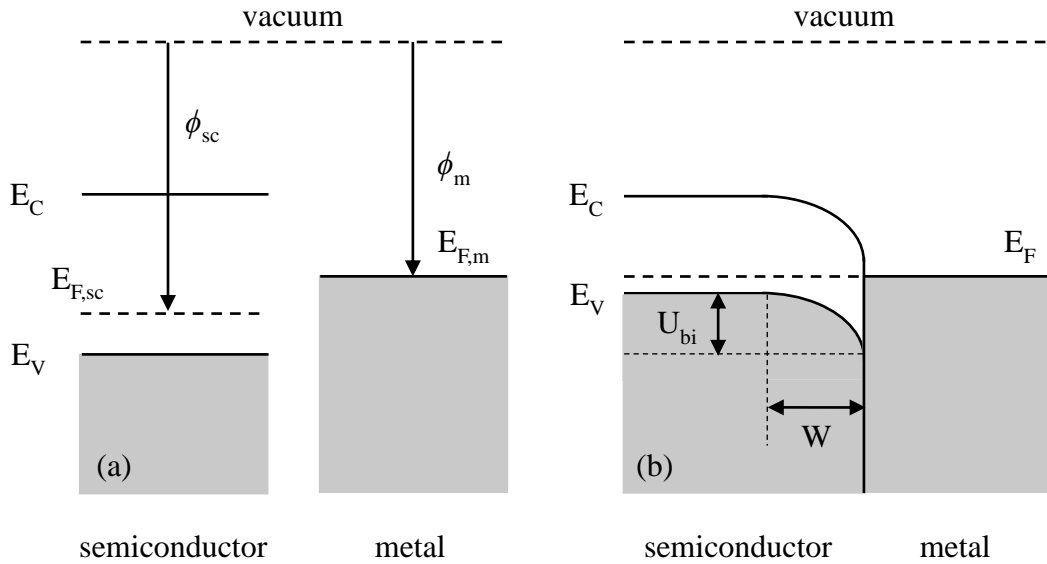


Figure 5: Energy band diagram of a metal and p-type semiconductor not in contact (a) and in contact (b).

When a contact between the metal and the semiconductor is formed (see figure 5(b)), charges will move across the interface and a thermodynamic equilibrium is reached by the aligning of the Fermi levels  $E_{F,m}$  and  $E_{F,sc}$ . A depletion layer ( $W$ ) is formed in the semiconductor region near the contact, which is depleted of charge carriers. By applying a negative voltage, the depletion layer gets bigger and the current will decrease.

The displayed built-in voltage ( $U_{bi}$ ) in figure 5 (b) equals the potential across the depletion region in thermal equilibrium and can be obtained from a Mott-Schottky plot. A Mott-Schottky plot shows the capacity of a device at certain voltages, which has been measured at a certain frequency. The built-in voltage is given by the extrapolated intersection with the voltage axis. [9]

## 2.4 Poole-Frenkel field dependence

The dependence of the carrier mobility  $\mu$  of hopping holes or electrons on the electric field  $E$  follows the Poole-Frenkel-type field dependence,  $\log \mu \propto \beta E^{1/2}$ . Where  $\beta$  is the Poole-Frenkel coefficient. When the  $\log \mu$  is plotted against  $E^{1/2}$ , an increase or decrease of the mobility with increasing field can be observed. Hereby, the Poole-Frenkel coefficient  $\beta$  can be determined by the slope of a linear fit. It is stated that the typical  $\log \mu \propto \beta E^{1/2}$  field dependence of the mobility vanishes at certain temperatures ( $T > T_0$ ), which leads to a negative  $\beta$  [11]. This

behaviour is described by Gill [12] according to the following equation, where  $\mu_0$  is the mobility at  $T_0$ ,  $\Delta$  is the zero-field activation energy,  $k_B$  is the Boltzmann constant, and  $T_{\text{eff}} = T - T_0$ .

$$\mu(T, E) = \mu_0 \exp \left[ -\frac{\Delta - \beta E^{1/2}}{k_B T_{\text{eff}}} \right] \quad (3)$$

Furthermore, the charge transport in disordered organic semiconductors is described by hopping in a material with energetic ( $\sigma/(k_B T)$ ) and positional disorder ( $\Sigma$ ) with Gaussian distribution functions, which is presented through the following equation:

$$\mu(T, E) = \mu_0 \exp \left[ -\frac{2}{3} \left( \frac{\sigma}{k_B T} \right)^2 \right] \exp \left\{ -C \left[ \left( \frac{\sigma}{k_B T} \right)^2 - \Sigma^2 \right] E^{1/2} \right\}, \quad (4)$$

where  $\sigma$  is the width of the Gaussian density of states,  $\mu_0$  is a prefactor mobility in the energetic disorder-free system, and  $C$  is a fit parameter. [11,13]

In case of equation (4), the slope of the electric field dependence of the mobility decreases with increasing electric field and turns to negative when  $\sigma/(k_B T) < \Sigma$ . A negative field dependence can occur in a system of large positional disorder, where a charge carrier can avoid a jump over a large energy barrier by finding a more favourable detour. These alternative detour paths can involve a jump against the field direction. At higher field these paths are blocked, which results in many dead-ends for charge carriers and therefore to a decrease in the charge mobility with increasing field. [14]

### **3. Experimental Section**

In this thesis three organic solar cells with a different active layer composition were produced and investigated. One has only P3HT, another one a blend of P3HT and five weight-percent PCBM and the third one has a blend of P3HT/PCBM in a 1:1 (*m:m*) ratio as an active layer. This section gives an insight into the production procedure and the used equipment for measuring the devices.

#### **3.1 Production procedure**

All devices were produced in the same manner. Changes in the production procedure for single devices are discussed separately.

First of all the needed polymer solution must be prepared a day before spin coating. The materials are weighed in a 3 mL flask and dissolved in Chlorobenzene, where they are stirred with a magnetic bar at 70 °C over night. All solutions are prepared with a concentration of 40 mg/mL.

The first step is to cut the Indium-Tin-Oxide (ITO) glass into 1.5 x 1.5 cm plates, which is the considered standard size for small solar cell substrates. Then a certain area of the substrate is covered with tape to define the remaining ITO layer. This step is critical since after the etching of the ITO layer the remaining conductive area directly affects the active area of the produced organic solar cell. Therefore, a quarter of the substrate is covered with tape and placed into a bath of conc. 37 % HCl for 5 minutes. After the etching the substrates are washed with deionized water and dried with compressed N<sub>2</sub>.

Afterwards the substrates are placed in a teflon sample holder, which is submerged into a cleaning agent called Hellmanex III. The samples are placed in an ultrasonic bath for 30 minutes at 80 °C and afterwards washed with deionized water. In addition, the samples are cleaned in acetone and isopropanol each for 15 minutes in the ultrasonic bath at room temperature and again dried with compressed N<sub>2</sub>. As a standard procedure, the substrates are treated in a Plasma ETCH P25 – plasma oven with O<sub>2</sub> at 50 W for 5 minutes. This step increases the surface tension of the substrates and additionally removes all remaining organic impurities.

The treated substrates are spin coated with a solution of Polyethyleneimine (PEI) (0.2% in 1-Butanol):1-Butanol (1:5) with a speed of 4000 rpm for 30 seconds and then annealed for

5 minutes at 105 °C. To receive comparable samples with a similar active layer thickness, the rotation speed at which the polymer solution is spin coated has to be adjusted for each solution. To retain a layer thickness of 150 nm, the solution with P3HT must be spin coated at 2000 rpm for 20 seconds, the solution with P3HT and five weight-percent PCBM at 5000 rpm for 20 seconds as well as the solution with P3HT/PCBM (1:1) at 5000 rpm for 20 seconds. Afterwards all samples are again annealed for 5 minutes at 105 °C.

A small area above the ITO layer must be cleaned with a piece of cotton and toluene before the electrodes can be evaporated onto the substrate. The samples are installed in a thermal evaporator (Univex 350) and 10 nm MoOx and 100 nm Ag are evaporated on the substrates. After the evaporation, the samples are stored in the glovebox under nitrogen atmosphere. The general layer structure of the solar cell, as well as a finished organic solar cell which is ready for measurements can be seen in figure 6.

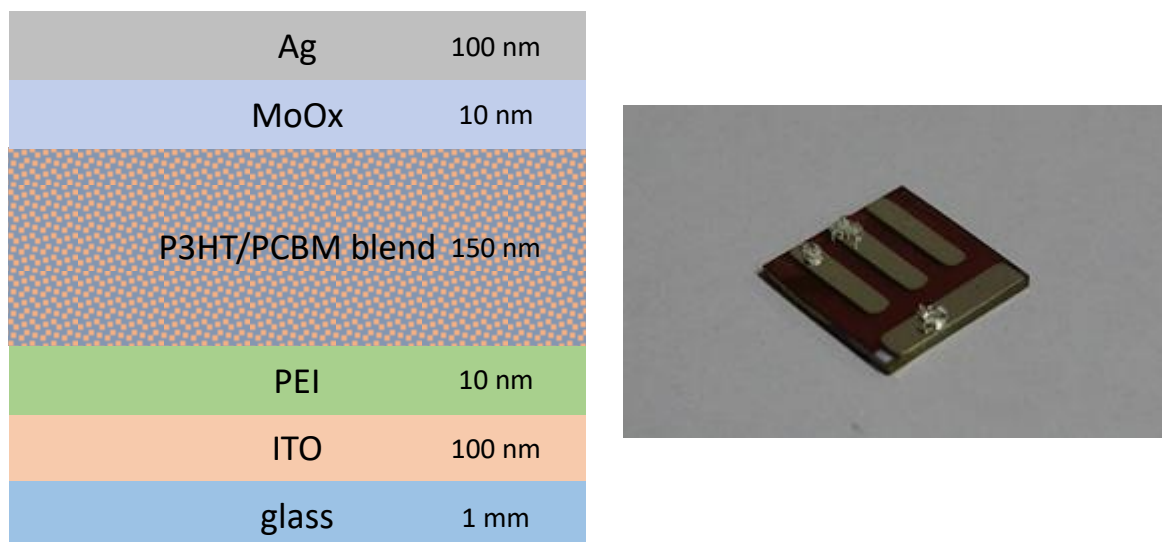


Figure 6: Layer composition of the processed solar cells (left). Finished solar cell with P3HT as active layer (right).

## 3.2 Equipment

### 3.2.1 Cryostat

A closed cycle cryostat was used to make precise temperature-dependent measurements between 180 K and 300 K. This cryostat is cooled with liquid helium. The helium flows constantly into the cryostat, where a built-in heater regulates the temperature to the programmed value. The temperature can be adjusted over the cryostat control panel. During measurements, a Pfeiffer Turbo Cube is creating a vacuum in the chamber of the cryostat to ensure an air free atmosphere. Measured samples are cooled down in 10 K steps. After the programmed temperature is reached, an additional 5 minutes were waited to ensure that the substrate has completely equilibrated to the temperature. In figure 7 displays a picture of the used cryostat.

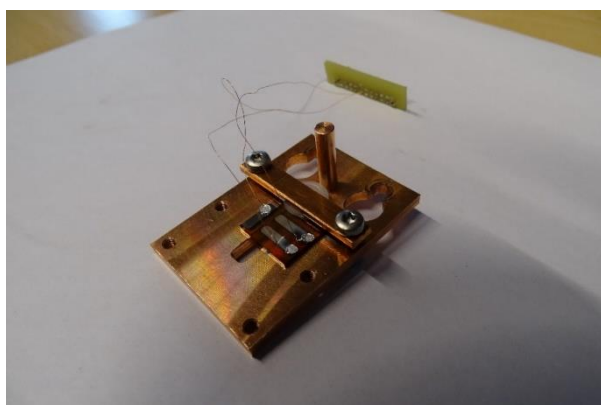


Figure 7: Oxford Instrument cryostat with helium in- and outlet (top) and vacuum connection (bottom).

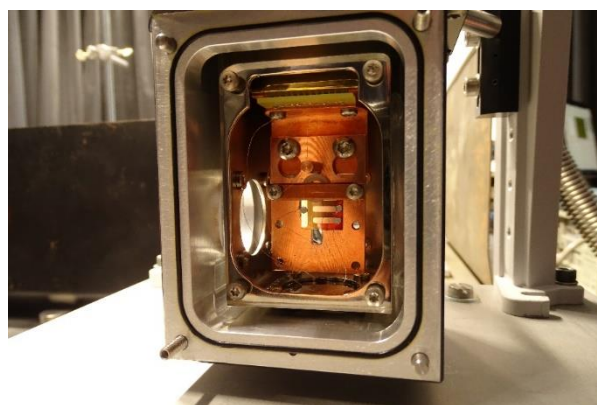
### 3.2.2 Installation of the solar cell

First a connection between the sample and the outside connectors must be established. In this thesis a DRYLX20 connector was used, which fits into the socket inside the cryostat chamber. The connector board and the cells of the substrate are connected through a thin copper wire, which is soldered onto the connector pins and the cell with indium. This connector board

enables to work outside of the cryostat chamber and therefore contributes to a simple and quick installation of the device. The organic solar cell is placed on a copper plate with a slit and tightened with a small copper bar. In figure 8 (a) a picture of a connected solar cell on a copper plate is displayed. The whole apparatus is installed in the cryostat by screwing the plate into the chamber and by plugging the connector into the socket. In figure 8 (b) the installed solar cell is shown.



(a)



(b)

Figure 8: (a) Installed and connected solar cell on a copper plate. (b) Installed and connected sample inside the cryostat chamber.

### 3.2.3 Apparatus for Photo-CELIV measurements

All measurements are conducted on a ThorLabs optical table, which is surrounded by a large black curtain. In figure 9 the whole equipment for the measurements is visible. Sensitive equipment like the cryostat, the laser as well as mirrors and lenses are mounted on the table.

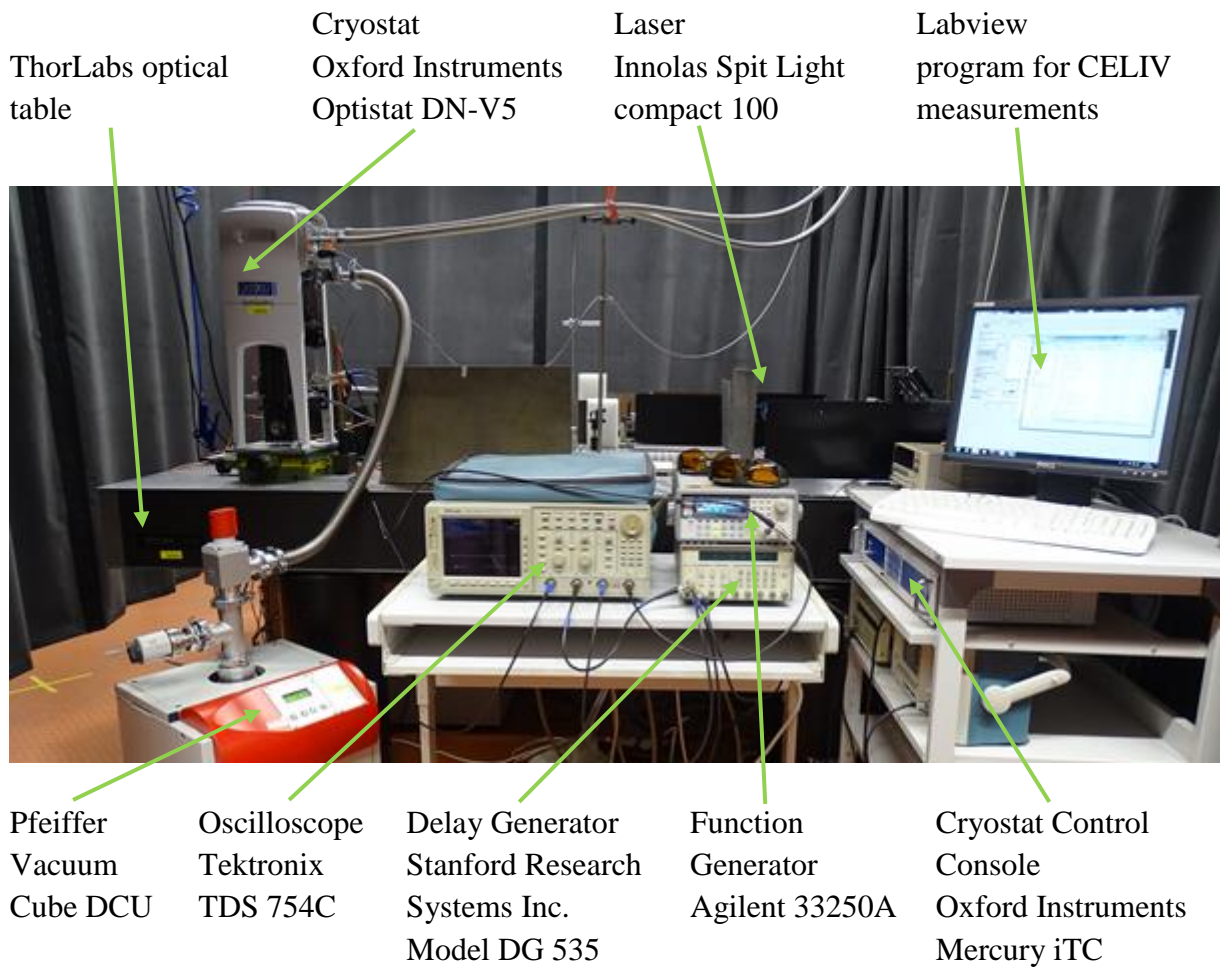


Figure 9: Relevant equipment used for photo-CELIV measurements.

The illumination light comes from a Nd:YAG laser, which is pulsed at 10 Hz (pulse-duration = 10 ns) and has an energy-density of  $3000 \mu\text{J}/\text{cm}^2$ . Different neutral density filters were applied to adjust the illumination intensity. The cryostat console controls the built-in heater and the temperature sensors in the cryostat and regulates the current of the heater to the adjusted temperature.

For photo-CELIV measurements a voltage ramp must be applied on the sample in backwards direction. First a silicon reference diode (ThorLabs DET 110), which is activated by the

pulsed laser light, triggers the delay generator. The delay generator adjusts the delay of the voltage ramp to the laser signal and triggers the function generator, which applies a defined voltage ramp over time on the cell. The oscilloscope is connected with all devices including the cell and measures the changing voltage of the sample over time. The described equipment is connected to the computer and can be controlled over the Labview program. The schematic setup for the photo-CELIV measurements is displayed in figure 10.

It is important to know that no shutter was used to partially reflect light of the laser pulse onto the diode during the experiments. The diode was placed next to the laser, which emitted enough scattering light to trigger the diode. Therefore, the displayed shutter in figure 10 is to show the theoretical setup.

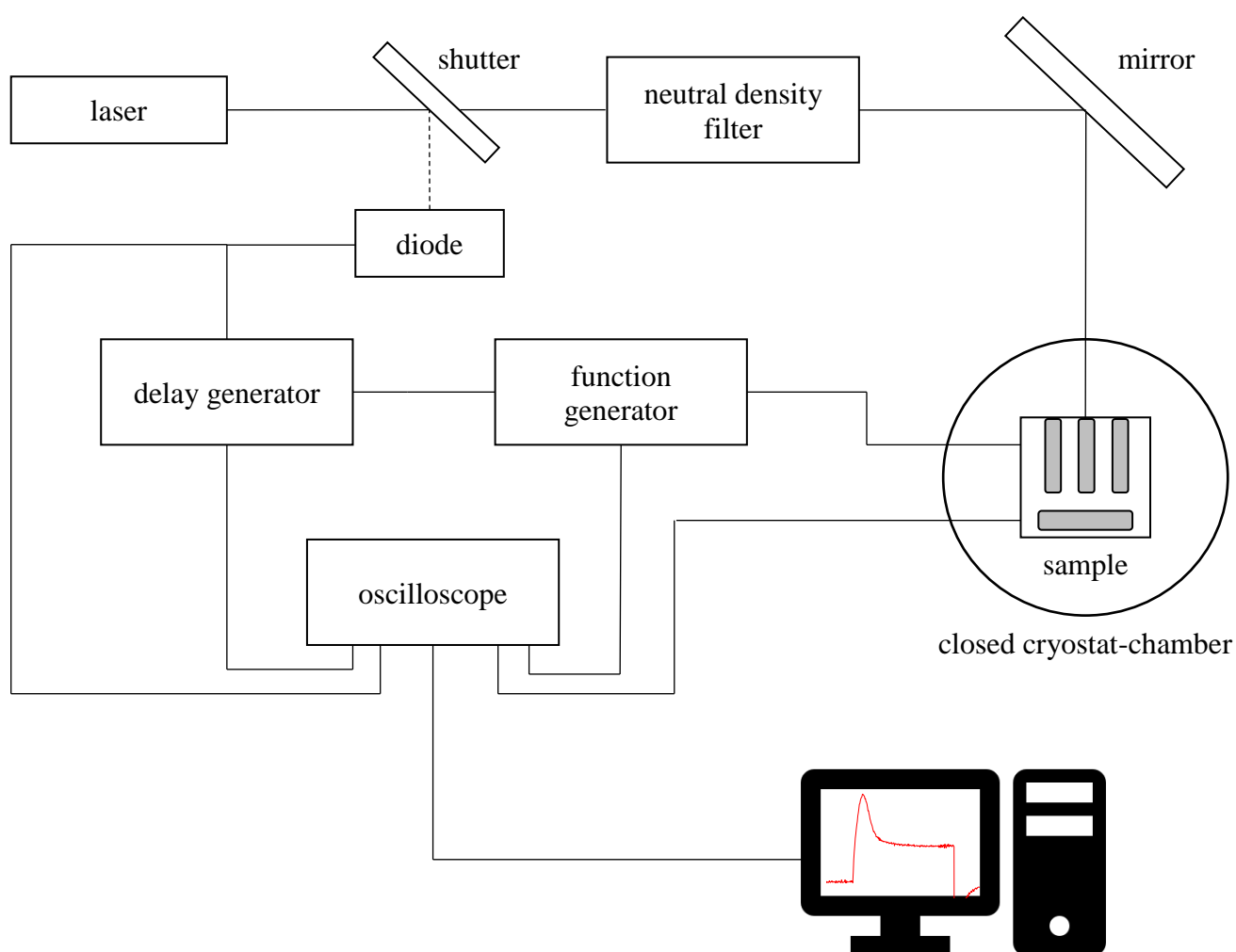


Figure 10: Schematic setup for measuring photo-CELIV of all organic solar cells with the basic connection paths between the utilized equipment.

## 4. Measurements and results

In this section the behaviour of a pure P3HT, P3HT/PCBM (0.95:0.05) and P3HT/PCBM (1:1) bulk heterojunction solar cell is investigated.

### 4.1 Pure P3HT-film

#### 4.1.1 JV characteristics of a pure P3HT film

The JV measurements were conducted inside the glovebox with a solar simulator emitting  $100 \text{ mW/cm}^2$ , AM 1.5 G. The P3HT film has a thickness of 150 nm and an area of  $2.77 \text{ mm}^2$ . These measurements are conducted to define the open circuit voltage ( $V_{oc}$ ) as well as the short-circuit current-density ( $J_{sc}$ ), efficiency ( $\eta$ ) and the fill factor ( $FF$ ). In figure 11 a JV-diagram of a pure P3HT film is displayed.

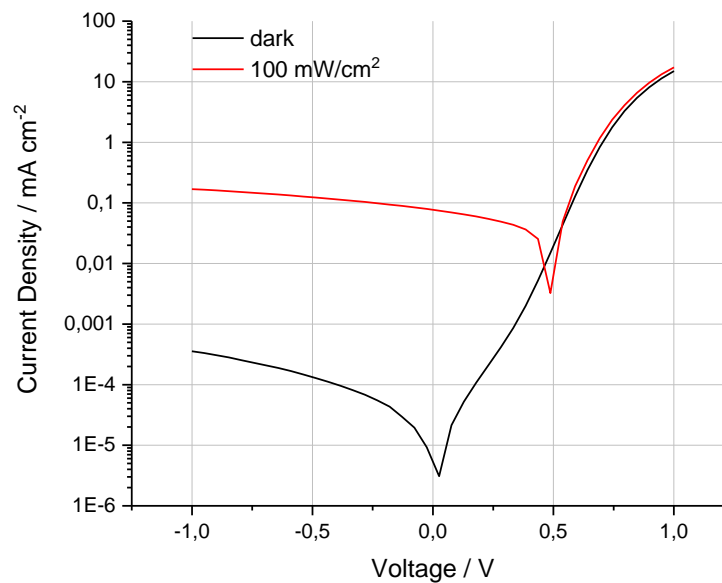


Figure 11: JV measurement of a pure P3HT film. Current in log scale, voltage in linear scale.

Without illumination (dark) the JV curve shows a very low current in reverse direction. Upon illumination with  $100 \text{ mW/cm}^2$  an open circuit voltage of nearly 0.5 V is noticeable. The above figure shows that the device is working. The  $J_{sc}$  is with  $0.1 \text{ mA/cm}^2$  low, nevertheless this behaviour is expected since there is no PCBM in the device, which would act as an acceptor and increase the current.

### 4.1.2 Mobility in P3HT films

The mobility in all devices was measured with the photo-CELIV method. The P3HT device was installed in the cryostat as mentioned in 3.2.2 and measured with the setup in figure 9. A pulsed laser with 532 nm was used as a light source. A voltage of 5 V, as well as a voltage ramp-duration ( $t_{del}$ ) of 20  $\mu$ s was primarily used for all measurements.

To receive reliable data from the setup, every device has to be analysed under certain conditions. Therefore, parameters like voltage, delay, offset voltage, illumination intensity and temperature were varied throughout the measurements.

#### 4.1.2.1 Dependency on delay and voltage

The delay is the time between the laser-pulse and the beginning of the extraction of the light induced charge carriers by an applied voltage. The longer the delay, the less charge carriers are extracted because of favoured recombination. This is shown in figure 12 (a), where the current-density is plotted against time with various delays.

The amount of applied voltage is important to ensure that all generated charge carriers can be extracted. The differences in the current-density by changing the voltage is shown in figure 12 (b).

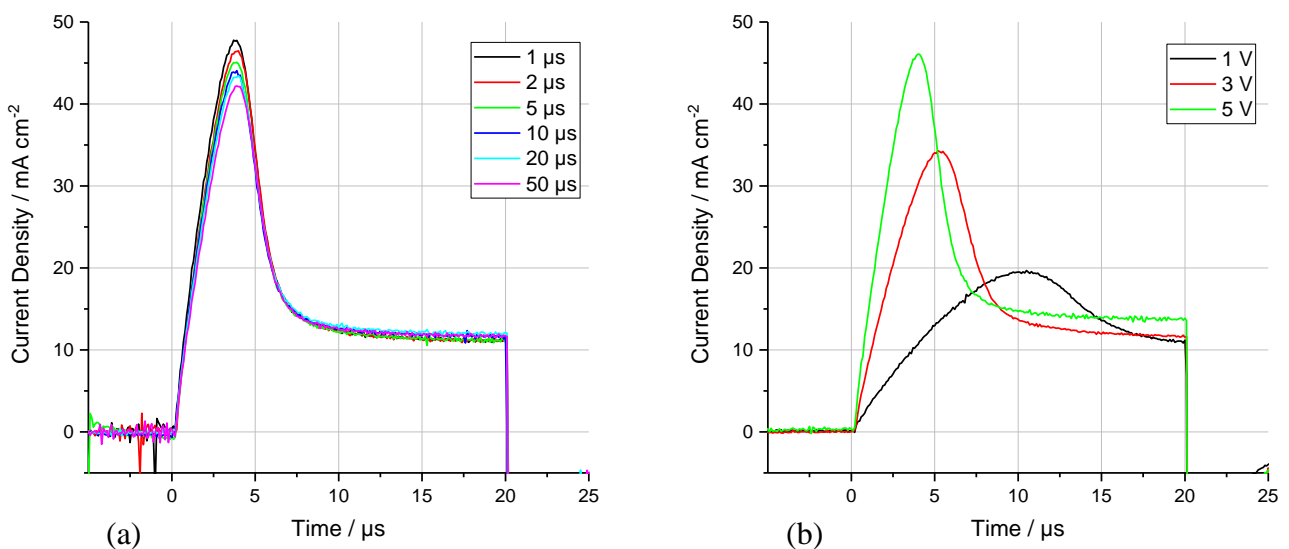


Figure 12: (a) Photo-CELIV diagram of a pure P3HT film at different delays (300  $\mu$ J/cm<sup>2</sup>, 5 V). (b) Photo-CELIV diagram of a pure P3HT film at different voltages (300  $\mu$ J/cm<sup>2</sup>,  $t_{del}$  = 20  $\mu$ s).

As displayed in figure 12 (b) a voltage of 1 V or 3 V is not favourable for the extraction of all charge carriers. This is indicated by the decreasing current-density between 15  $\mu\text{s}$  and 20  $\mu\text{s}$ . In general, a linear behaviour towards the end of the extraction is favoured (e.g. 5 V), which indicates that all light generated charge carriers have been extracted.

#### 4.1.2.2 Dependency on the offset voltage

To prevent an early extraction or injection of the charge carries, the offset voltage ( $V_{off}$ ) has to be manually adjusted to the used illumination intensity. A correctly adjusted offset voltage acts like a barrier for the generated charge carries before the extraction point (0  $\mu\text{s}$ ) and leads to quantitatively correct evaluation of the photo-CELIV signal.

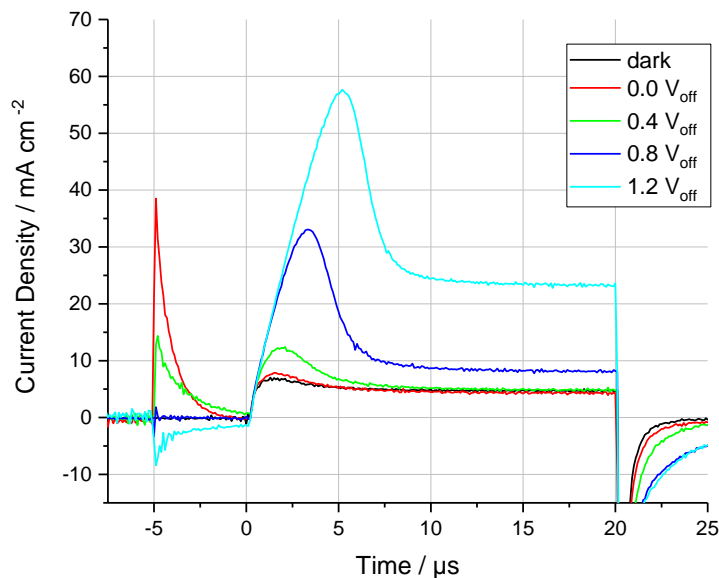


Figure 13: Photo-CELIV diagram of a P3HT film at 30  $\mu\text{J}/\text{cm}^2$  and 5 V with different offset voltages.

The effects of different  $V_{off}$  applied, on the device are shown in figure 13. It is seen that an offset voltage of 0 V and 0.4 V show large peaks before the extraction point. In this case, the applied voltage is too small so charge carriers are extracted, which leads to a weakened photo-CELIV signal. If the offset voltage is too high (e.g. 1.2 V), charge carriers are injected and the photo-CELIV signal gets amplified. The plot with  $V_{off} = 0.8$  V shows none of the before mentioned peaks and is therefore considered to be correct.

### 4.1.2.3 Dependency of the mobility on the illumination intensity

The effects of changing illumination intensities on the current of a P3HT film can be seen in figure 14 (a). In figure 14 (b) the differences of the calculated carrier mobility values with different illumination intensities are displayed. Figure 14 (c) presents a different plot compared to figure 14 (b), where the change of the mobility with increasing illumination intensities at different delays is displayed in a double-log plot.

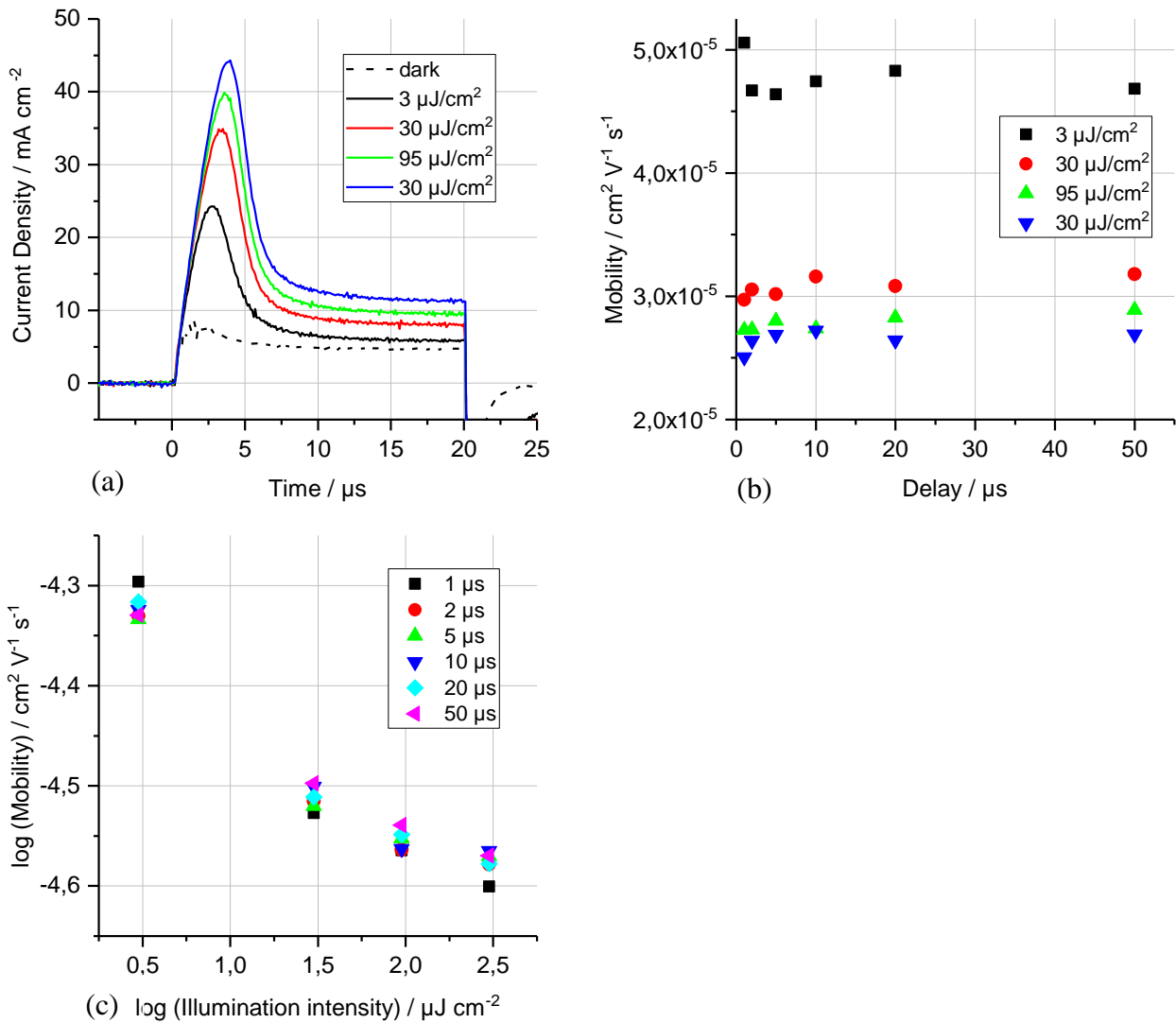


Figure 14: (a) Photo-CELIV diagram of the P3HT- film, at different illumination intensities (5 V,  $t_{det} = 20 \mu\text{s}$ ). (b) Calculated mobility values for every illumination intensity and delay at 300 K (5 V). (c) Double logarithmic plot of the mobility of the charge carriers vs the illumination intensity at different delays (300 K, 5 V).

Figure 14 (a) shows that the maximum of the current and therefore the value for  $t_{max}$  increases with increasing illumination intensities. Additionally, the ratio of  $\Delta j$  and  $j(0)$  changes slightly

with varying illumination intensities. As a consequence to an increasing  $t_{max}$  value, the mobility of the charge carriers has to decrease according to equation (2). This can be seen in figure 14 (b), since the calculated mobility values at e.g.  $300 \mu\text{J}/\text{cm}^2$  are slightly smaller than the others. The same behaviour can be seen in figure 14 (c), where the mobility of the charge carriers nearly decreases linearly with increasing illumination intensities. However, the mobility values for  $30, 95,$  and  $300 \mu\text{J}/\text{cm}^2$  are in the same range.

Although the illumination intensity of  $3 \mu\text{J}/\text{cm}^2$  shows a deviation from all others in terms of the mobility, it is still considered to be correct. The calculated values are a factor of two higher and are still in the same order of magnitude. Illumination intensities between  $30 - 300 \mu\text{J}/\text{cm}^2$  show nearly identical results for the mobility with a mean value of  $2.8 \cdot 10^{-5} \text{ cm}^2/\text{V s}$  at  $20 \mu\text{s}$ .

#### 4.1.2.4 Dependency of the mobility on the temperature

To investigate the dependency of the mobility on the temperature, a series of measurements was conducted. The device was cooled down from  $300 \text{ K}$  to  $180 \text{ K}$  in  $10 \text{ K}$  steps. Once the device reached the adjusted temperature it was measured with a variation of the mentioned parameters.

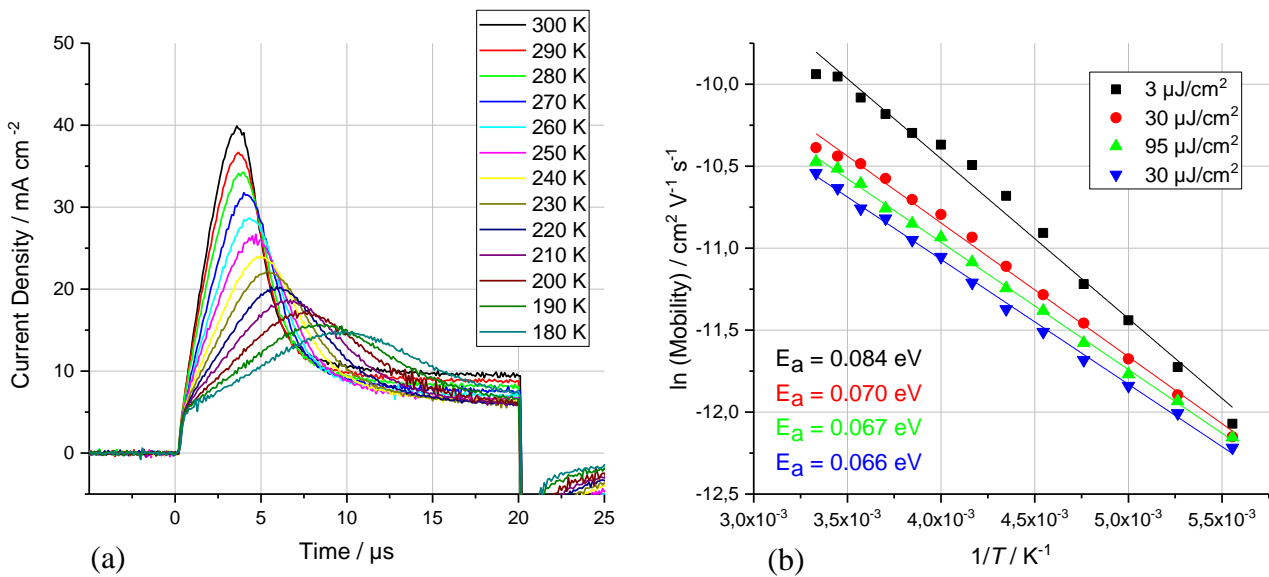


Figure 15: (a) Photo-CELIV diagram of P3HT at different temperatures ( $95 \mu\text{J}/\text{cm}^2$ ,  $5 \text{ V}$ ,  $t_{del} = 20 \mu\text{s}$ ). (b) Arrhenius plot of the mobility vs temperature at different illumination intensities ( $5 \text{ V}$ ,  $t_{del} = 20 \mu\text{s}$ ).

In figure 15 (a) a decrease of the current-density as well as a shift of the peak maximum (increasing  $t_{max}$ ) with decreasing temperature is noticeable. This behaviour is expected since the charge carriers are slowed down and cannot be fully extracted, which leads to an overall smaller mobility. In figure 15 (b) the change of the mobility at different temperatures and illumination intensities is presented via an Arrhenius plot. The activation energy for each illumination intensity can be calculated by multiplying the slope of the linear fit with the negative Boltzmann constant ( $k_B$ ). In most cases the slope is negative, which results in a positive value for the activation energy when multiplied with  $-k_B$ . As displayed in figure 15 (b), the activation energies decrease with increasing illumination intensity, which is expected since more energy is provided to promote the separation of the electron and hole. It is noticed that the mobility of the charge carriers decreases in a linear way until it reaches a common point around  $5.3 \cdot 10^{-6} \text{ cm}^2/\text{V s}$ .

#### 4.1.3 Charge carrier concentration in P3HT films

The charge carrier concentration gives information about the amount of charge carriers that are extracted from one  $\text{cm}^3$  of the active layer. It can be easily calculated from the photo-CELIV data and gives further information about the transport processes inside the P3HT film.

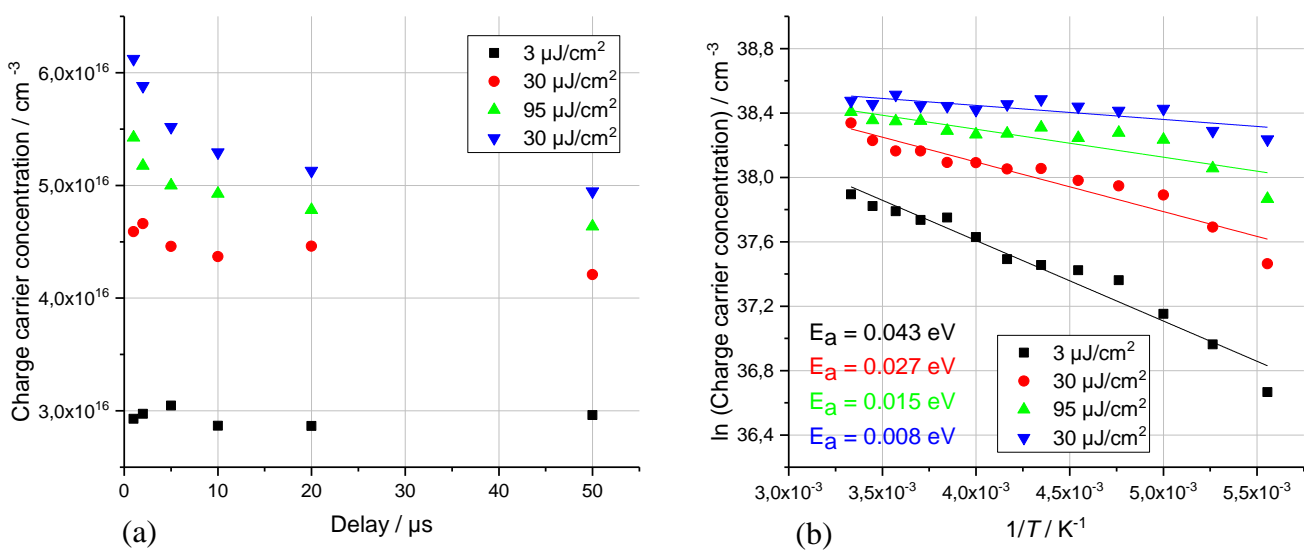


Figure 16: (a) Charge carrier concentration of P3HT vs delay at different illumination intensities (5 V, 300 K). (b) Arrhenius plot of the charge carrier concentration vs temperature at different illumination intensities (5 V,  $t_{del} = 20 \mu\text{s}$ ).

Figure 16 (a) shows the behaviour of the charge carrier concentration, depending on the increasing delay and at different illumination intensities. It is evident that the charge carrier concentration decreases with an increasing delay, whereas at 20  $\mu\text{s}$  and 50  $\mu\text{s}$  the difference is rather small. This behaviour is expected since with larger delays less light-induced charge carriers can be extracted because they have already recombined again. If the delay was too long, the photo-CELIV signal as well as the charge carrier concentration would be equal to a non-illuminated sample, where no additional charge carriers would be extracted.

In figure 16 (b) the decrease of the charge carrier concentration related to the temperature at different illumination intensities is pictured as an Arrhenius plot. It is observed that the amount of extracted charge carriers slightly decreases with decreasing temperature, especially for smaller illumination intensities. At 300  $\mu\text{J}/\text{cm}^2$  and 95  $\mu\text{J}/\text{cm}^2$  the change of the charge carrier concentration is rather small. It is further noticed that the activation energies decrease with increasing illumination intensities. Hereby the activation energy can be calculated like in 4.1.2.4 briefly explained.

## 4.2 P3HT/PCBM (0.95:0.05) Bulk Heterojunction Solar Cell

### 4.2.1 JV characteristics

The measured device has a thickness of 150 nm and an active area of 3.09 mm<sup>2</sup>. Measurements were taken with the same solar simulator as introduced in 4.1.1.

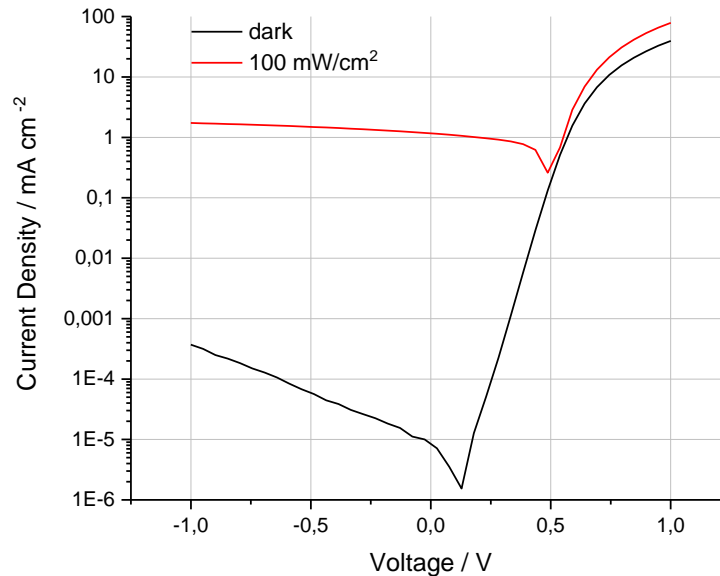


Figure 17: JV measurement of a P3HT/PCBM (0.95:0.05) film. Current in log scale, voltage in linear scale.

The JV curve in figure 17 has many similarities with the JV curve of a pure P3HT film (4.1.1). The leakage-current in the dark is very small and the open circuit voltage is 0.5 V upon illumination. With a five weight-percent of PCBM present in the film, a much higher  $J_{sc}$  of 1.2 mA/cm<sup>2</sup> is observed. The small addition of PCBM leads to an increase of the  $J_{sc}$  of 12 times, compared to the  $J_{sc}$  in a pure P3HT film (4.1.1).

## 4.2.2 Mobility

### 4.2.2.1 Dependency on delay and voltage

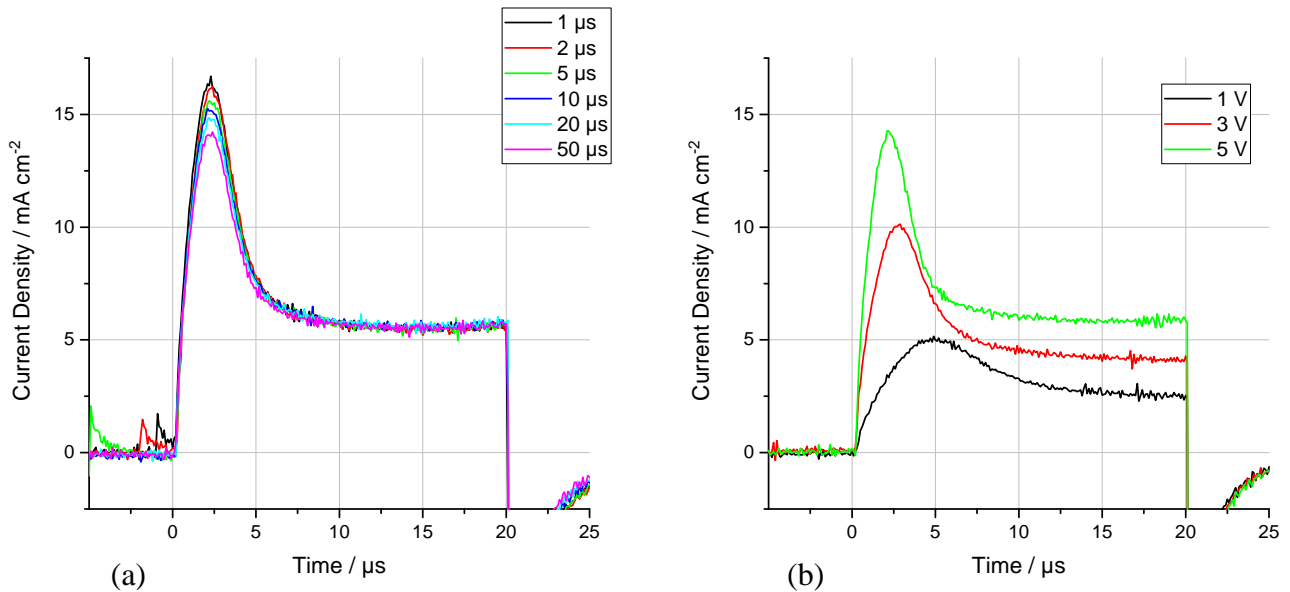


Figure 18: (a) Photo-CELIV diagram of a P3HT/PCBM (0.95:0.05) film at different delays ( $0.3 \mu\text{J}/\text{cm}^2$ , 5 V). (b) Photo-CELIV diagram of a P3HT/PCBM (0.95:0.05) film at different voltages ( $0.3 \mu\text{J}/\text{cm}^2$ ,  $t_{del} = 20 \mu\text{s}$ ).

Besides the decreasing current with increasing delay, a series of peaks before the extraction point ( $0 \mu\text{s}$ ) is noticeable in figure 18 (a). These peaks originate from the laser impulse, which creates charge carriers inside the film. Those charge carriers are extracted before the voltage ramp is applied, which would normally start the extraction of the charge carriers. It was found that an offset voltage of 560 mV was the highest amount that could be applied onto the device without injecting additional charge carriers. In subchapter 4.1.2.2 the need of a correctly adjusted offset voltage has been introduced.

Figure 18 (b) shows multiple photo-CELIV plots at different voltages. The plots with 1 V and 3 V do not show a constant behaviour towards the end and are therefore not favourable. Nevertheless the 5 V diagram shows a constant behaviour towards the end and is used for further mobility measurements.

#### 4.2.2.2 Dependency of the mobility on the illumination intensity

In this subchapter, the additional effects of the different illumination intensities on the introduced PCBM in the film are shown. Furthermore, the changes of the calculated mobility values are discussed.

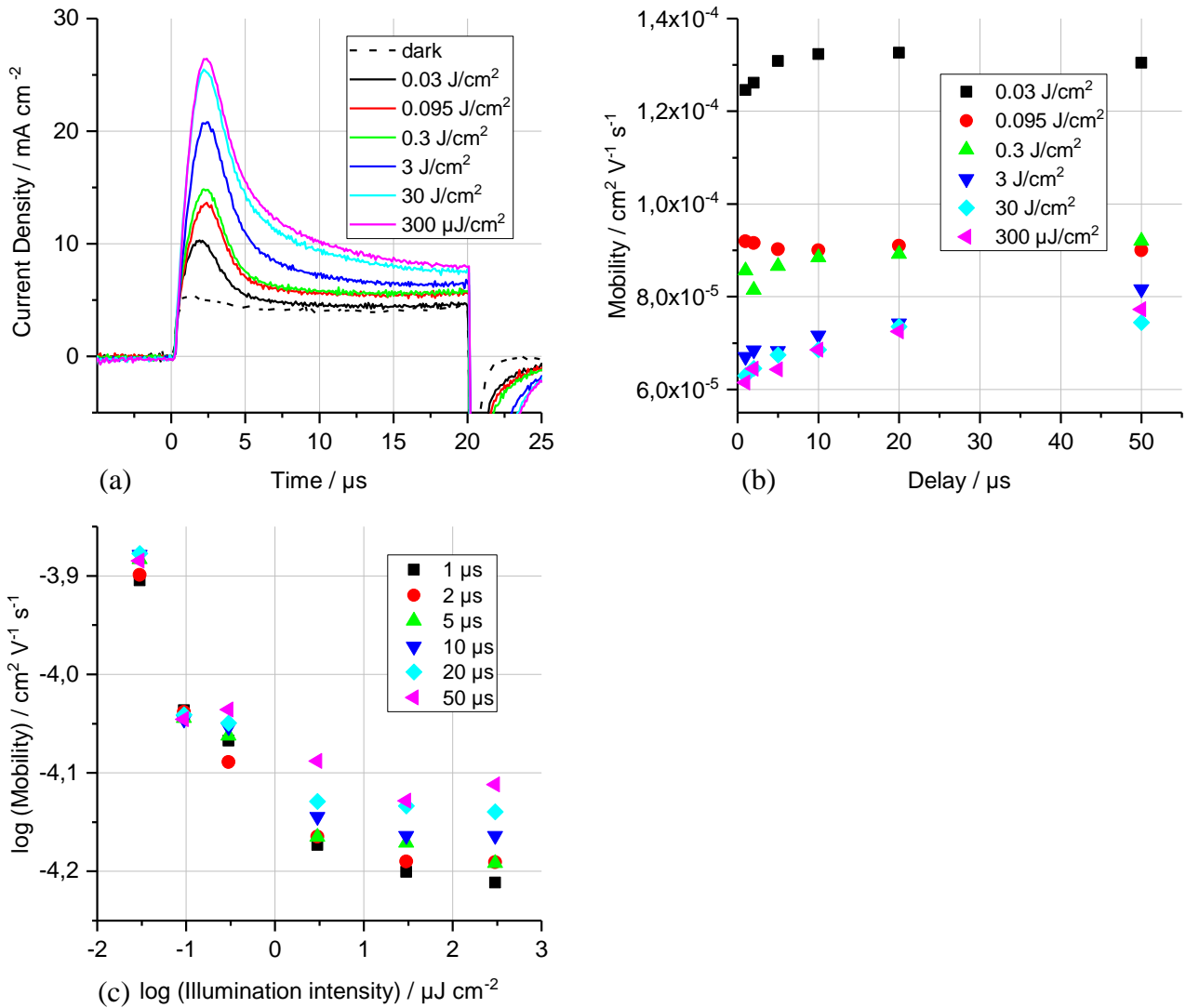


Figure 19: (a) Photo-CELIV diagram of P3HT/PCBM (0.95:0.05) at different illumination intensities (5 V,  $t_{del} = 20 \mu s$ ). (b) Calculated mobility values for every illumination intensity and delay at 300 K (5 V). (c) Double-logarithmic plot of the mobility of the charge carriers vs the illumination intensity at different delays (300 K, 5 V).

Figure 19 (a) shows a photo-CELIV diagram of the P3HT/PCBM film. A delay of 20  $\mu\text{s}$  and a voltage of 5 V was chosen for all given plots. It is observed that the graphs with 30  $\mu\text{J}/\text{cm}^2$  and 300  $\mu\text{J}/\text{cm}^2$  do not have a constant current towards the end of the extraction (20  $\mu\text{s}$ ). This implies that not all generated charge carriers are extracted, which concludes that the chosen ramp duration for the applied voltage is too short. Instead of changing the ramp duration, a lower illumination intensity of 0.3  $\mu\text{J}/\text{cm}^2$  is utilized to determine the mobility inside the film. In figure 19 (b) a linear trend for the mobility of the charge carriers is observed for smaller illumination intensities. Nevertheless, at higher illumination intensities, the mobility increases with a higher delay. As already mentioned above, the charge carriers cannot be fully extracted at higher illumination intensities, which simply means that a fraction of charge carriers is lost. Therefore, the mobility appears to be smaller at decreasing delays and upon higher illumination. Figure 19 (c) shows the decrease of the mobility with increasing illumination intensities at different delays. It is observed that the mobility does not decrease in a linear way like for the pure P3HT device, in figure 14 (c). In addition, the mobility of the charge carriers increases with increasing delay and decreasing illumination intensity, as mentioned in figure 19 (b).

Considering that 0.3  $\mu\text{J}/\text{cm}^2$  is the most suitable illumination intensity for the P3HT/PCBM (0.95:0.05) film, a mobility of  $8.9 \cdot 10^{-5} \text{ cm}^2/\text{V s}$  at 20  $\mu\text{s}$  is found.

#### 4.2.2.3 Dependency of the mobility on the temperature

In figure 20 (a) the behaviour of the current-density is displayed at different temperatures, which shows a constant decrease as well as a shift of the peak maximum and current-density correlating to a decreasing temperature. Between 200 K and 180 K the maximum of the peaks does not decrease in current-density but rather shifts on the time-axis towards higher  $t_{max}$  values.

The mobility of the charge carriers is decreasing constantly in a linear way with decreasing temperature. This is shown in figure 20 (b) and looks similar to the behaviour of the pure P3HT film (4.1.2.4). A mobility of the charge carriers of around  $9.3 \cdot 10^{-6} \text{ cm}^2/\text{V s}$  is reached at 180 K. In terms of the activation energy, the same behaviour is observed like for the P3HT device (4.1.2.4).

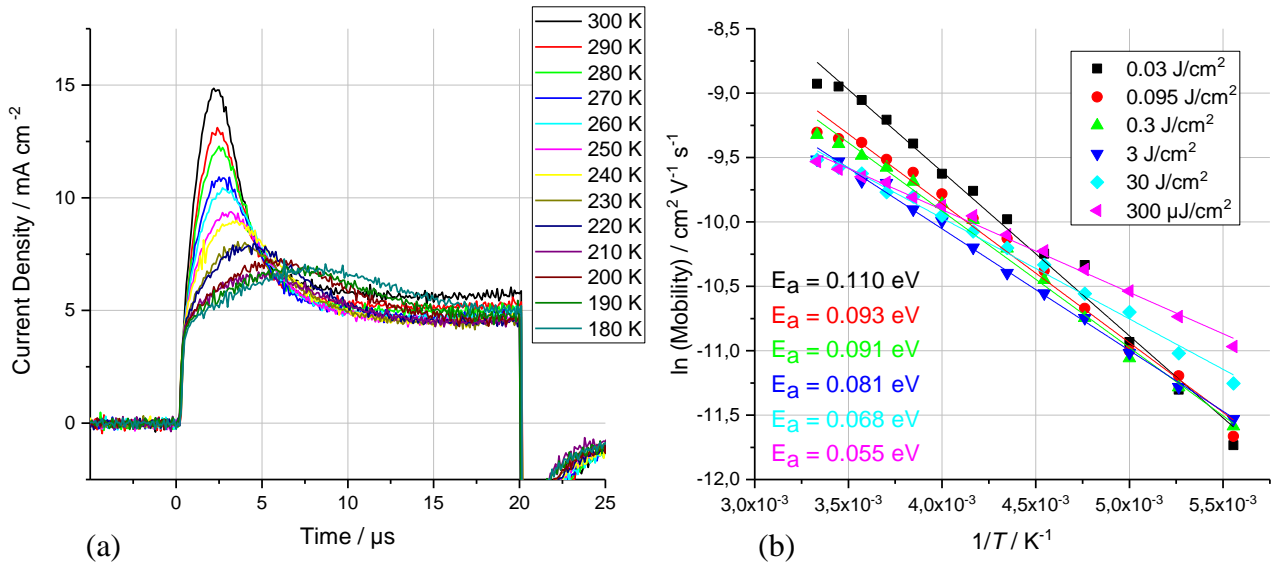


Figure 20: (a) Photo-CELIV diagram of P3HT/PCBM (0.95:0.05) at different temperatures ( $0.3 \mu\text{J}/\text{cm}^2$ ,  $5 \text{ V}$ ,  $t_{del} = 20 \mu\text{s}$ ). (b) Arrhenius plot of the mobility vs temperature at different illumination intensities ( $5 \text{ V}$ ,  $t_{del} = 20 \mu\text{s}$ ).

### 4.2.3 Charge carrier concentration

The P3HT/PCBM film shows a similar behaviour in its charge carrier concentration, as for a pure P3HT film (4.1.3). In figure 21 (a) a steep decrease of the charge carrier concentration with increasing delays is observed for higher illumination intensities. Compared with the charge carrier concentration of the pure P3HT film at  $30 \mu\text{J}/\text{cm}^2$  the P3HT/PCBM film has a 1.5 times smaller charge carrier concentration at a given delay of  $20 \mu\text{s}$ . It is simply smaller because the two films are not completely comparable since not all charge carriers of the P3HT/PCBM film can be extracted at  $30 \mu\text{J}/\text{cm}^2$  and the film shows some minor defects, as previously mentioned.

Figure 21 (b) shows the calculated charge carrier concentration at different temperatures and various illumination intensities. It is observed that the charge carrier concentration is mainly constant with decreasing temperature for higher illumination intensities. In terms of lower illumination intensities, only a small deviation is visible. Moreover, figure 21 (b) shows a negative activation energy for  $3$ ,  $30$ , and  $300 \mu\text{J}/\text{cm}^2$ , which is a result of the positive slope of the linear fit of the calculated data. This can be approximately explained by looking at figure 18 (a), which shows that a small amount of charge carriers is extracted before the extraction point ( $0 \mu\text{s}$ ). This leads to a reduced amount of charge carriers that can be extracted during the

intended extraction period (0-20  $\mu\text{s}$ ), which directly lowers the calculated charge carrier concentration. As one can expect, this effect increases with an increasing illumination intensity, since more charge carriers are generated before the extraction. However, this effect decreases with decreasing temperature. It is therefore suggested that the charge carrier concentration for 3, 30, and 300  $\mu\text{J}/\text{cm}^2$  would be higher at higher temperatures, which would lead to a linear fit with a negative slope and therefore to a positive value for the activation energy, which would correlate with the found behaviour in figure 16 (b).

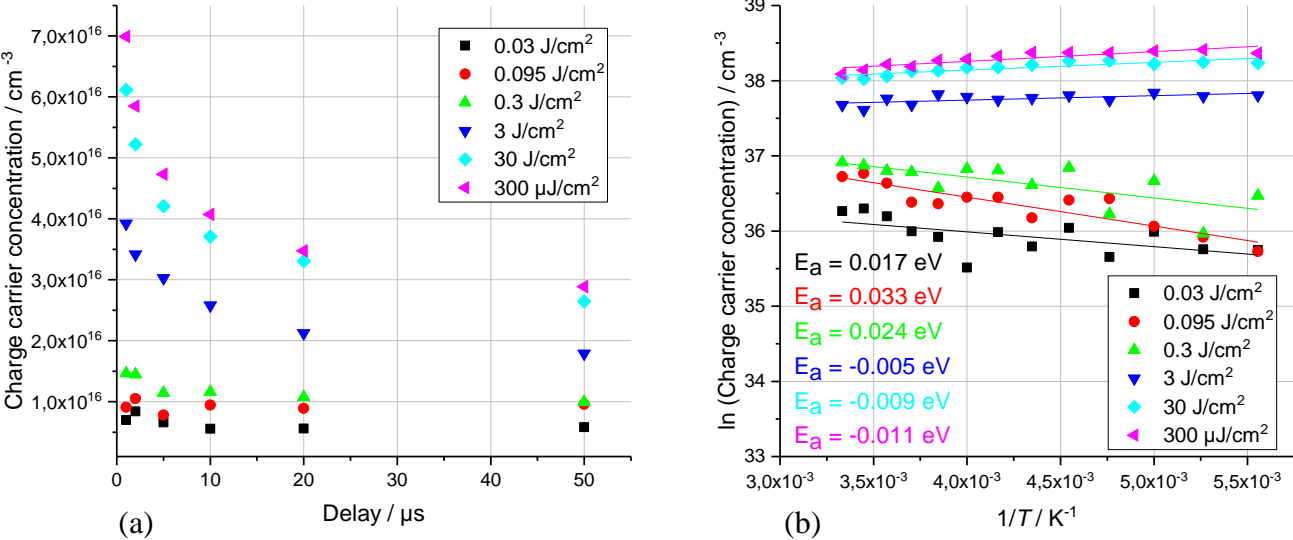


Figure 21: (a) Charge carrier concentration vs delay at different illumination intensities (5 V, 300 K). (b) Arrhenius plot of the charge carrier concentration vs temperature at different illumination intensities (5 V,  $t_{del} = 20 \mu\text{s}$ ).

## 4.3 P3HT/PCBM (1:1) Bulk Heterojunction Solar Cell

### 4.3.1 JV characteristics

In this subchapter, a JV diagram of the P3HT/PCBM (1:1) bulk heterojunction solar cell is presented in figure 22 and onwards discussed. The device has a thickness of 150 nm and an active layer area of 4.33 mm<sup>2</sup>.

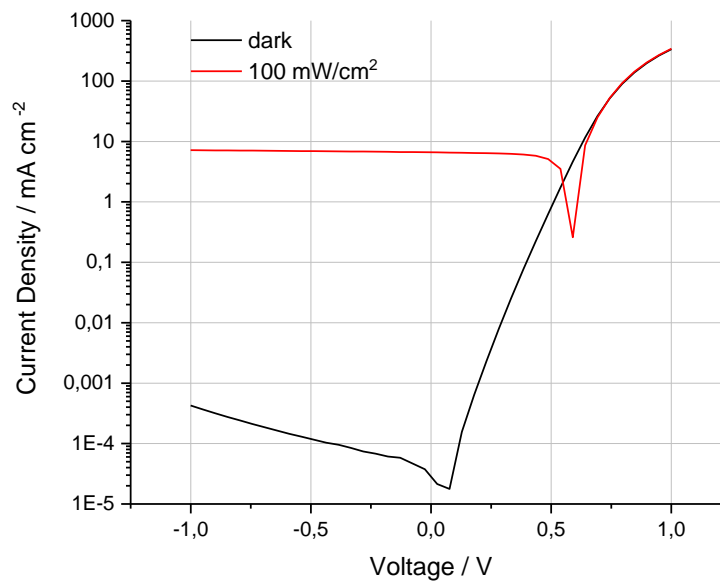


Figure 22: JV measurement of a P3HT/PCBM (1:1) film. Current in log scale, voltage in linear scale.

The film shows the same characteristics as those of the pure P3HT and P3HT/PCBM (0.95:0.05) film. Nevertheless, a larger open circuit voltage of 0.59 V is observed upon illumination with 100 mW/cm<sup>2</sup>. In addition, it is found that the device has a  $J_{sc}$  of 6.6 mA/cm<sup>2</sup>, which is nearly 6 times higher than the  $J_{sc}$  of the P3HT/PCBM (0.95:0.05) film. The enhanced  $J_{sc}$  originates from the addition of PCBM into the active layer film. It contributes to the overall charge separation and charge transport inside the film.

## 4.3.2 Mobility

### 4.3.2.1 Dependency on voltage and delay

The dependency of the P3HT/PCBM (1:1) on the delay and the applied voltage shows no major deviations from the previous mentioned devices. Yet, it can be seen that in figure 23 (a) the intensity of the peaks before 0  $\mu\text{s}$  is much higher than in figure 18 (a). At this stage, the bulk heterojunction solar cell produces a lot more current because of the 1:1 ratio of P3HT and PCBM. To overcome those peaks, an offset voltage (mentioned in 4.1.2.2) has to be applied. In this case, a  $V_{\text{off}}$  of 0.6 V was applied.

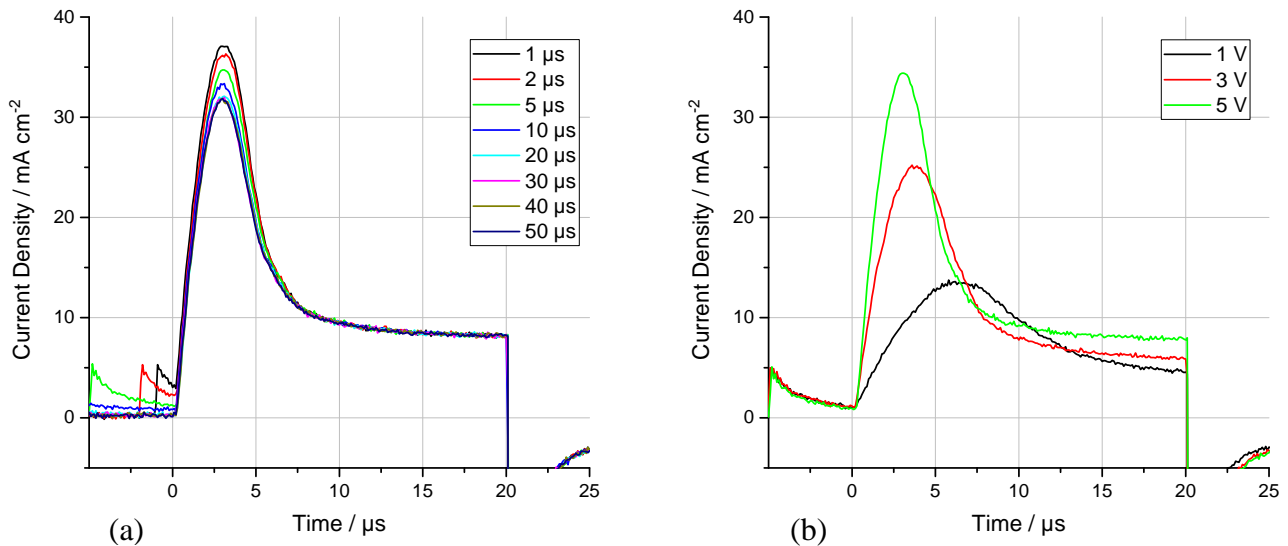


Figure 23: (a) Photo-CELIV diagram of a P3HT/PCBM (1:1) film at different delays ( $0.3 \mu\text{J}/\text{cm}^2$ , 5 V). (b) Photo-CELIV diagram of a P3HT/PCBM (1:1) film at different voltages ( $0.3 \mu\text{J}/\text{cm}^2$ ,  $t_{\text{del}} = 5 \mu\text{s}$ ).

In figure 23 (b) the photo-CELIV-signal at different voltages is displayed. As mentioned in 4.2.2.1 the plots for 1 V and 3 V do not show a constant behaviour towards the end, which means that not all charge carriers are extracted. However, 5 V seem to be enough to extract all charge carriers. The previously discussed matter with the increased peaks before the extraction point (0  $\mu\text{s}$ ), is also visible in this figure.

### 4.3.2.2 Dependency of the mobility on the illumination intensity

The charge separation and transport is highly enhanced in a P3HT/PCBM (1:1) bulk heterojunction solar cell compared to a pure P3HT film (4.1.2.3) or a P3HT film with a small amount of PCBM (4.2.2.2). Therefore, the extracted current-density is very large at higher illumination intensities. This is seen in figure 24 (a) where the peaks before the extraction point, as well as the peak maxima, are very large.

During the measurements, it was observed that the  $V_{off}$  could not be adjusted in a way that additional charge carriers would not be injected. Therefore, an offset voltage of 0.6 V was used throughout all measurements with the device.

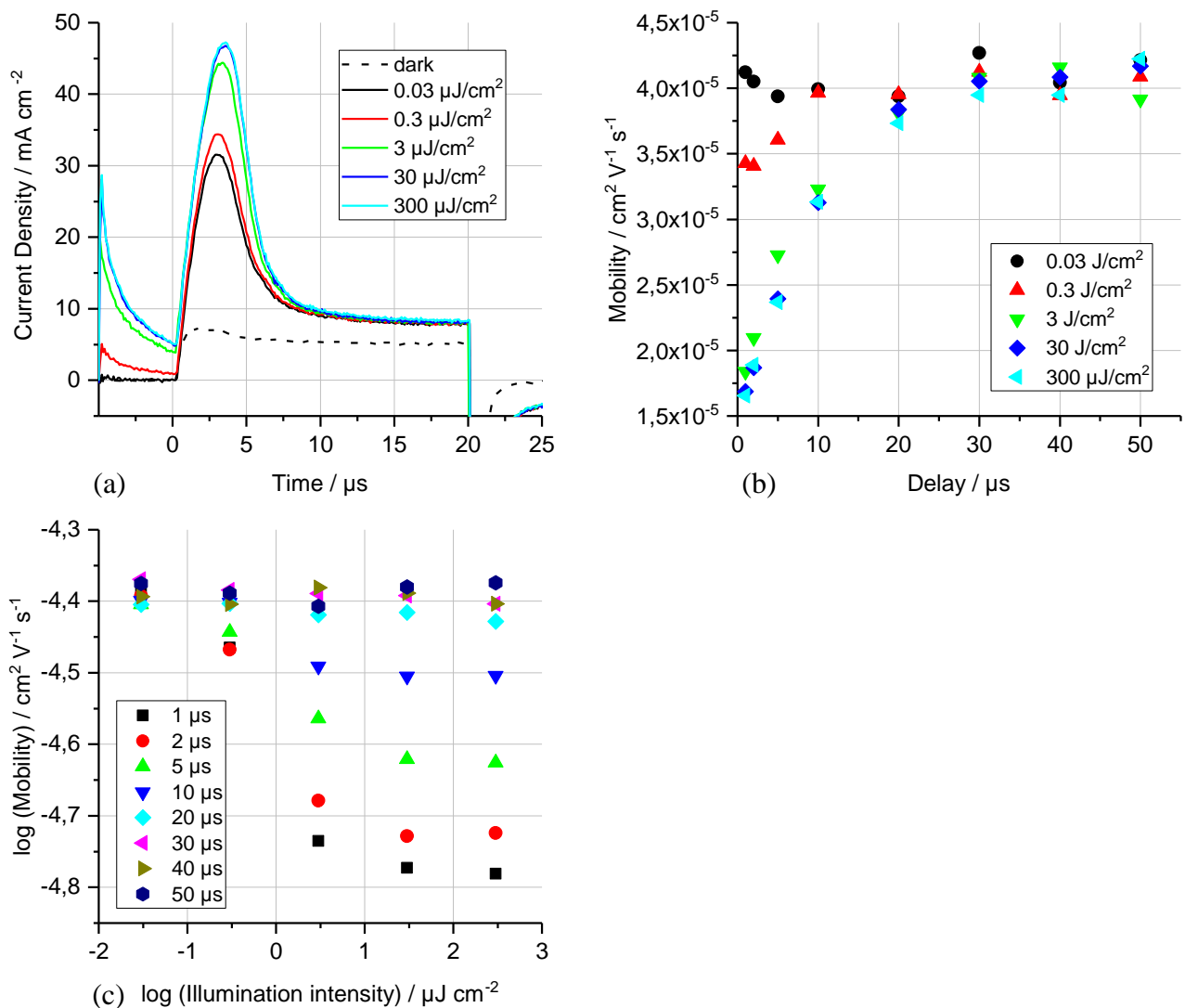


Figure 24: (a) Photo-CELIV diagram of P3HT/PCBM (1:1) at different illumination intensities (5 V,  $t_{del} = 5 \mu$ s). (b) Calculated mobility values for every illumination intensity and delay at 300 K (5 V). (c) Double-logarithmic plot of the mobility of the charge carriers vs the illumination intensity at different delays (300 K, 5 V).

In figure 24 (b) similarities with the device in section 4.2 are observed. The mobility of the charge carriers increases with the increasing delay at higher illumination intensities, which is a result of the charge carrier loss before the extraction point (figure 24 (a)). Since a majority of the charge carriers are extracted beforehand, all remaining charge carriers are extracted between the applied voltage ramp duration ( $0\mu\text{s}$  -  $20\mu\text{s}$ ). It is observed in figure 24 (c) that the mobility of the charge carriers decreases with increasing illumination intensities for short delays. Since a shorter delay increases the loss of charge carriers before the extraction point, it is only reasonable that the mobility of the charge carriers decreases too. It is also noted that the calculated value for the mobility is constant with increasing illumination intensities, when a delay higher than  $20\mu\text{s}$  is selected for the measurement.

The mobility of the charge carriers lies within the range of  $3.5\cdot 10^{-5}\text{ cm}^2/\text{V s}$  to  $4.5\cdot 10^{-5}\text{ cm}^2/\text{V s}$ , which is nearly twice as high as for a pure P3HT film. Nevertheless, it is also smaller than the mobility value for the P3HT/PCBM (0.95:0.05) film, which can only be a result of the above discussed issues.

#### **4.3.2.3 Dependency of the mobility on the temperature**

The P3HT/PCBM (1:1) film shows the same behaviour as the devices mentioned in 4.1.2.4 and 4.2.2.3, while being measured at temperatures from 300 K to 180 K. In figure 25 (a) the decrease of the current-density with the decrease of temperature is displayed. Figure 25 (b) shows the decreasing mobility values with decreasing temperature. It is noticed that the mobility of the charge carriers only decreases at a very small rate. In addition, the plots for the higher and lower illumination intensities are separated from each other. This is because of the loss of charge carriers at the delay ( $t_{del}$ ) of  $5\mu\text{s}$ , which is discussed in 4.3.2.2.

It is observed that the activation energy seems to increase with increasing illumination intensities, which is contrary to the observed behaviour for both other devices. This trend is observed, because the slope of the linear fit of the data decreases with increasing illumination intensity. As suggested in 4.3.2.2, a fast amount of charge carriers could not be extracted before the extraction point ( $0\mu\text{s}$ ), which leads to an overall decreased value for the mobility of the charge carriers. It is concluded that this effect becomes more relevant, when higher illumination intensities are utilized. However, the produced device with P3HT/PCBM (1:1) generates a lot of charge carriers upon illumination, which leads to the necessity of using a

rather low illumination intensity to overcome the effect of losing charge carriers before the extraction point.

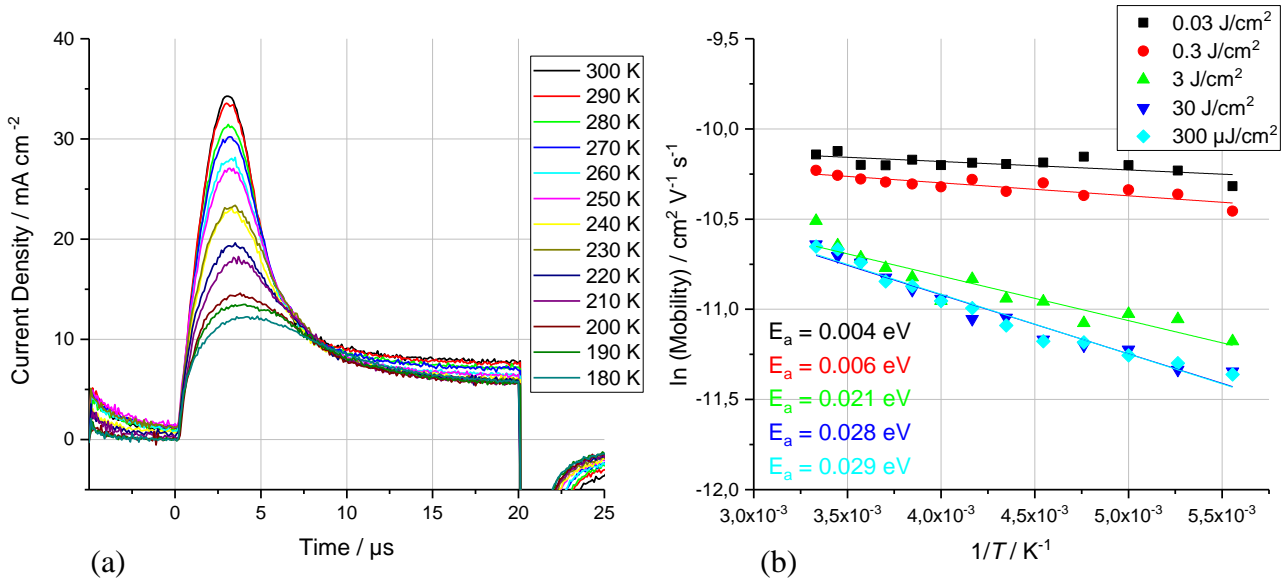


Figure 25: (a) Photo-CELIV diagram of P3HT/PCBM at different temperatures ( $0.3 \mu\text{J}/\text{cm}^2$ ,  $5 \text{ V}$ ,  $t_{del} = 5 \mu\text{s}$ ). (b) Arrhenius plot of the mobility vs temperature at different illumination intensities ( $5 \text{ V}$ ,  $t_{del} = 5 \mu\text{s}$ ).

Nevertheless, the mobility of the charge carriers in the film is in a magnitude of  $1.2 \cdot 10^{-5} \text{ cm}^2/\text{V s}$  to  $3.5 \cdot 10^{-5} \text{ cm}^2/\text{V s}$  at  $180 \text{ K}$ , which is much higher than in the other investigated films. This shows that the charge carrier transport in the film is still high under low temperatures. The mobility inside the film might be much higher if all charge carriers could have been fully extracted.

#### 4.4.3 Charge carrier concentration

In terms of charge carrier concentration, the P3HT/PCBM (1:1) film shows similar behaviour like the film discussed in 4.2.3. Compared to figure 21 (a), figure 26 (a) also shows the same decreasing trend of the charge carrier concentration with increasing delays for higher illumination intensities. Nevertheless, in figure 26 (a) all plots reach a common point with roughly  $4.0 \cdot 10^{16} \text{ cm}^{-3}$  at higher delays, which is larger than the value for the device in 4.2.3. It is suggested that the constant applied  $V_{off}$  of  $0.6 \text{ V}$  leads to a constant loss of charge carries

before the intended extraction. This could also be a reason for the linearity of  $t_{max}$ , which is seen for all plots in subchapter 4.3.2.3, figure 25 (a).

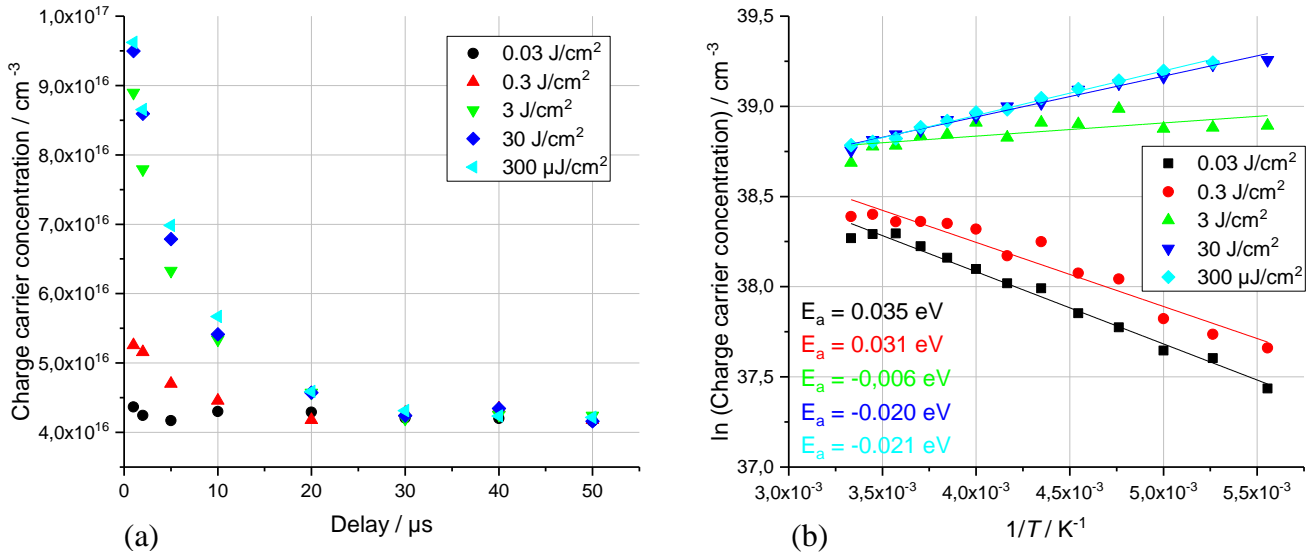


Figure 26: (a) Charge carrier concentration vs delay at different illumination intensities at (5 V, 300 K). (b) Arrhenius plot of the charge carrier concentration vs temperature at different illumination intensities (5 V,  $t_{del} = 20 \mu s$ ).

Figure 26 (b) also shares great similarities with figure 21 (b). The charge carrier concentration is for  $3 \mu J/cm^2$  mostly constant over temperature, however shows a decrease with decreasing temperature for lower illumination intensities and an increase with decreasing temperature for larger illumination intensities. For the plots with higher illumination intensities, it is arguable whether the charge carrier concentration should increase with decreasing temperature. As mentioned in 4.2.3, it is more likely that due to the loss of charge carriers before the intended extraction-period (chapter 4.3.2.2), the charge carrier concentration is lower at higher temperatures. Whereas for lower temperatures this effect becomes less relevant.

#### 4.4 Impedance spectroscopy: Mott-Schottky plot

All measurements were conducted in the dark with 20 mV AC signal voltage with frequencies between 0.1 Hz and 10 MHz and with different DC bias voltages between -2 V and 1 V.

The figure (27) below shows the  $1/C_p^2$  versus the voltage with a frequency of  $1.13 \cdot 10^3$  Hz at room temperature. With this diagram one can determine the built-in voltage of the device by connecting the measured points with a straight line and cross the voltage-axis, where  $1/C_p^2$  is zero. The value of the crossing point on the voltage-axis gives the built-in voltage.

For the three processed devices, the built-in voltage is between 0.4 V and 0.5 V. The capacity of a device is among other parameters dependent on the thickness and the area of the active layer.

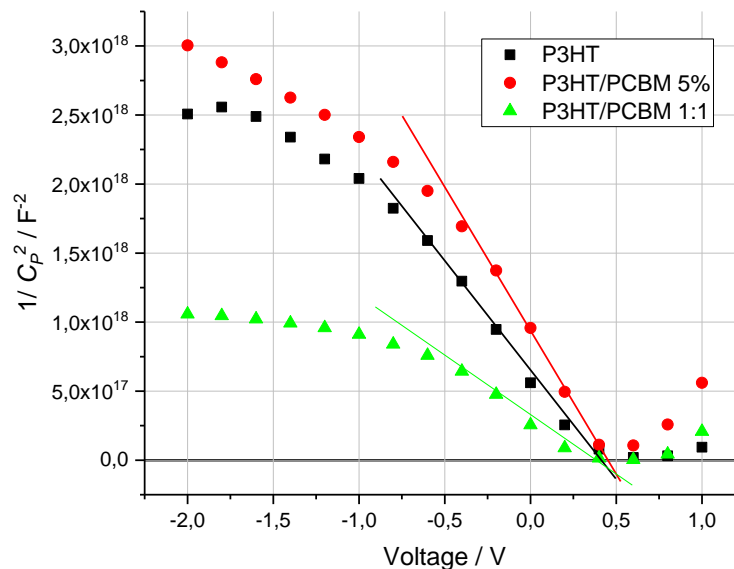


Figure 27: Mott-Schottky plot: Measured capacitance of all three devices vs voltage at RT without illumination ( $f = 1.13 \cdot 10^3$  Hz).

## 4.5 Poole-Frenkel field dependence in all devices

The Poole-Frenkel field dependence of the mobility  $\mu$  is investigated for all three processed devices. The mobility of the charge carriers in figure 12 (b), 18 (b), and 23 (b) is calculated for different applied voltages (1, 3, and 5 V) at room temperature and plotted against the square root of the electric field  $E$ . Figure 28 shows the  $\log \mu$  plotted against  $E^{1/2}$  where the Poole-Frenkel coefficient  $\beta$  can be determined by the linear fit, according to  $\log \mu \propto \beta E^{1/2}$  (chapter 2.4). In this case, the electric field  $E$  (V/cm) is calculated as suggested in [15] by the following equation, whereas  $A$  (V/s) is the slope of the applied voltage ramp,  $t_{max}$  (s) is the time between the extraction start and the current-density maximum, and  $d$  (cm) is the thickness of the active layer.

$$E_{t max} = \frac{A \cdot t_{max}}{d} \quad (5)$$

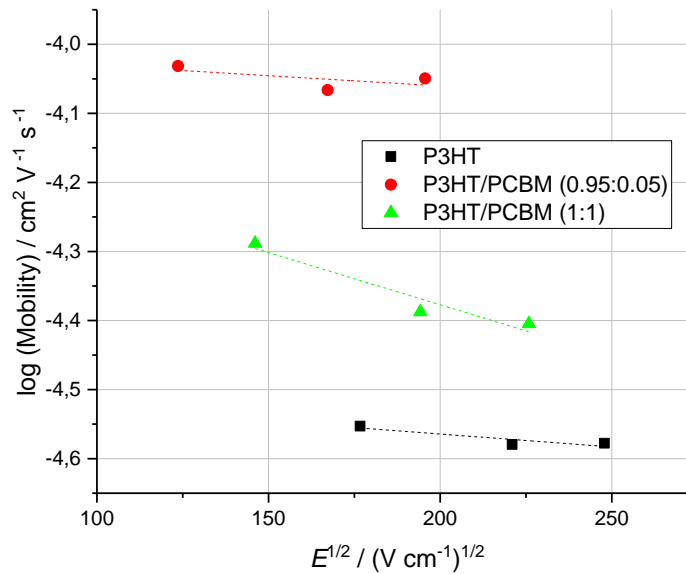


Figure 28: Poole-Frenkel field dependence plot, where  $\log \mu$  of all three processed devices is plotted against  $E^{1/2}$  at 300 K. The linear fit (dotted lines) of the mobility shows the behaviour of the Poole-Frenkel coefficient  $\beta$ .

As presented in figure 28, all three devices show a negative Poole-Frenkel coefficient at 300 K, as it is reported in [11]. However, it is observed that  $\beta$  appears to be more negative for the P3HT/PCBM (1:1) device. This may be a result of the loss of charge carriers before the

extraction point (discussed in chapter 4.2.3 and 4.4.3), which leads to several errors for the calculation of the mobility of the charge carriers. Due to the limited number of measurement points the Poole-Frenkel coefficient can only be estimated. For an accurate determination, more experimental points would be required.

## 5. Conclusion

A personal insight into the topic of bulk heterojunction solar cells and organic semiconductors has been obtained during this work. It ranges from the production of bulk heterojunction solar cell devices with thin films of P3HT and P3HT/PCBM, to their characterization (JV) by using a solar simulator, as well as to the investigation of the mobility of the charge carriers and the charge carrier concentration by using the photo-CELIV technique. Furthermore, the built-in voltage of these devices has been investigated by using impedance spectroscopy.

The three produced devices with a P3HT, P3HT/PCBM (0.95:0.05), and P3HT/PCBM (1:1) ( $m:m$ ) active layer show expected behaviours when comparing the JV diagrams. The device with only P3HT (donor) as an active layer, has a very low  $J_{sc}$  upon illumination. The increased addition of PCBM (acceptor) in the active layer film increases the  $J_{sc}$ , as well as the open circuit voltage ( $V_{oc}$ ). Since the generated exciton in the P3HT layer needs PCBM as an acceptor to perform charge separation, it is only reasonable that the increased amount of PCBM increases the charge separation and transport in a bulk heterojunction solar cell.

By using the photo-CELIV method, the mobility of the charge carriers and the charge carrier concentration in all three films is explored. Hereby, a wide range of parameters (e.g. delay, voltage, illumination intensity, temperature) are varied to obtain a spectrum of results, which is discussed in depth. It is noticed that the extraction of all generated charge carriers is achieved when using a higher voltage. For P3HT a hole-mobility of  $2.8 \cdot 10^{-5} \text{ cm}^2/\text{V s}$  at 300 K is found, which is in the range of reported values. With the addition of five weight-percent PCBM to the processing solution, an increase of the mobility of the charge carriers to  $8.9 \cdot 10^{-5} \text{ cm}^2/\text{V s}$  is noticed, which is the result of the established donor-acceptor interface in the active layer of the device. On the other hand, a lower mobility value of around  $4.0 \cdot 10^{-5} \text{ cm}^2/\text{V s}$  is found for the P3HT/PCBM (1:1) device. In theory, the increased amount of PCBM should increase the mobility of the charge carriers, since an increased area of the

donor-acceptor interface is formed. Nevertheless, this effect was not observed during this work due to some possible minor defects in the device and the not compensable extraction of charge carriers before the extraction point with the applied offset voltage ( $V_{off}$ ) (see 4.3.2.2).

In terms of temperature dependency, it is found that the mobility of the charge carriers decreases with decreasing temperature, which is expected. It is also noticed that the overall mobility for the P3HT/PCBM (1:1) device at 180 K is higher than the mobility of the charge carriers of the other two devices. In fact, the P3HT/PCBM (0.95:0.05) device has still a higher mobility than the P3HT device at 180 K, which shows that the PCBM strongly contributes to the charge transport even at low temperatures.

As for the charge carrier concentration of the three devices, it is found that it decreases with increasing delay, which is expected, since the photo-generated charge carriers start to recombine again. The results show that the charge carrier concentration of the P3HT device is between delays of 1  $\mu$ s to 5  $\mu$ s smaller than for the other devices. However, not all charge carriers of the P3HT/PCBM (0.95:0.05) and P3HT/PCBM (1:1) films could be extracted during the applied voltage ramp, because due to the utilized offset voltage some were extracted before the extraction point.

Regarding temperature dependency of the charge carrier concentration, it is found that it stays constant at decreasing temperatures, although some minor deviations for very small and/or very high illumination intensities occur. Nevertheless, this behaviour is mainly observed for the investigated P3HT/PCBM (1:1) device, which has possibly been affected by some of the addressed issues.

## 6. Bibliography

- [1] Yi-Bing Cheng, A. Pascoe, F. Huang, Y. Peng: *Print flexible solar cells*, Nature, 2016, Vol. 539, 488-489
- [2] M. Graetzel, R. A. J. Janssen, D. B. Mitzi, E. H. Sargent: *Materials interface engineering for solution-processed photovoltaics*, Nature, 2012, Vol. 488, 304-312
- [3] C. W. Tang: *Two-layer organic photovoltaic cell*, Appl. Phys. Lett. 48, 183 (1986)
- [4] J. Piris, T. E. Dykstra, A. A. Bakulin, P. H.M. van Loosdrecht, W. Knulst, M. T. Trinh, J. M. Schins, L. D.A. Siebbeles: *Photogeneration and Ultrafast Dynamics of Excitons and Charges in P3HT/PCBM Blends*, J. Phys. Chem. C. 113 (2009), 14500-14506
- [5] M. C. Scharber, N. S. Sariciftci: *Efficiency of bulk-heterojunction organic solar cells*, Progress in Polymer Science 38, 2013, 1929-1940
- [6] G. Juška, K. Arlauskas, M. Viliūnas, J. Kočka, *Extraction Current Transients: New Method of Study of Charge Transport in Microcrystalline Silicon*, Phys. Rev. Lett. 84, 2000
- [7] M. Stephen, K. Genevičius, G. Juška, K. Arlauskas, R. C. Hiorns: *Charge transport and its characterization using photo-CELIV in bulk heterojunction solar cells*, Polymer International, 2017, Vol. 66, Issue 1, 13-25
- [8] J. Lorrmann, B. H. Badada, O. Inganäs, V. Dyakonov, C. Deibel: *Charge Carrier Extraction by Linearly Increasing Voltage: Analytic framework and ambipolar transients*, Journal of Applied Physics 108, 113705 (2010)
- [9] F. Fabregat-Santiago, G. Garcia-Belmonte, I. Mora-Seró, J. Bisquert, *Characterization of nanostructured hybrid and organic solar cells by impedance spectroscopy*, Physical Chemistry Chemical Physics 13, Issue 20, 2011, 9083
- [10] L. Kronik, Y. Shapira, *Surface photovoltage phenomena: theory, experiment, and applications*, Surface Science Reports 37, 1999, 1-206
- [11] A. J. Mozer, N. S. Sariciftci, *Negative electric field dependence of charge carrier drift mobility in conjugated, semiconducting polymers*, Chem. Phys. Lett. 389 (2004), 438-442
- [12] W. D. Gill, *Drift mobilities in amorphous charge-transfer complexes of trinitrofluorenone and poly-n-vinylcarbazole*, J. Appl. Phys. 43, 5033 (1972)

- [13] V. Kazukauskas, M. Pranaitis, V. Cyras, L. Sicot, F. Kajzar, *Negative mobility dependence on electric field in poly(3-alkylthiophenes) evidenced by the charge extraction by linear increasing voltage method*, Thin Solid Films 516 (2008), 8988-8992
- [14] A. Köhler, H. Bässler, *Electronic Processes in Organic Semiconductors: An Introduction*, Wiley-VCH, 2015, 231-234
- [15] A. J. Mozer, N. S. Sariciftci, A. Pivrikas, R. Österbacka, G. Juška, L. Brassat, H. Bässler, *Charge carrier mobility in regioregular poly(3-hexylthiophene) probed by transient conductivity techniques: A comparative study*, Physical Review B 71, 035214 (2005)

## **7. Acknowledgements**

I would like to thank o.Univ. Prof. Mag. Dr. DDr. H.c. Niyazi Serdar Sariciftci for introducing me to the Linzer Institute for Organic Solar Cells (LIOS), giving me the opportunity to work in this scientific field, and learn about other interesting topics from his group.

Special thanks to my supervisor Assoc. Prof. DI Dr. Markus Clark Scharber, for his guidance and kind words throughout the whole thesis. At the end of the day, his patience and systematic teaching made this thesis to what it is. I would also like to express my special gratitude to DI Herwig Heilbrunner who taught me how the photo-CELIV setup works and who always had an open ear for my questions.

I also want to thank Assoc. Univ. Prof. DI Dr. Martin Kaltenbrunner and Dipl.-Ing. Christian Siket from the Soft Matter Physics Institute, for helping me with the impedance measurements.

Finally, I would like to thank the whole LIOS group for their help and for interesting discussions concerning scientific and/or social topics. I had an amazing time during my stay at the Institute and I am thankful that I had the chance to take part in some of the special LIOS-traditions.